
Article:
Brown, A.J. orcid.org/0000-0002-3316-7240, Parsons, S.G. orcid.org/0000-0002-2695-2654, van Roestel, J. orcid.org/0000-0002-2626-2872 et al. (12 more authors) (2023) Photometric follow-up of 43 new eclipsing white dwarf plus main-sequence binaries from the ZTF survey. Monthly Notices of the Royal Astronomical Society, 521 (2). pp. 1880-1896. ISSN 0035-8711

https://doi.org/10.1093/mnras/stad612

MNRAS 000, 1–13 (2023) Preprint 23 February 2023 Compiled using MNRAS LATEX style file v3.0

Photometric follow-up of 43 new eclipsing white dwarf plus main-sequence binaries from the ZTF survey

Alex J. Brown,[1]★ Steven G. Parsons,[1] Jan van Roestel,[2] Alberto Rebassa-Mansergas,[3,4] Elmé Breedt,[5] Vik S. Dhillon,[1,6] Martin J. Dyer,[1] Matthew J. Green,[7] Paul Kerry,[1] Stuart P. Littlefair[1] Thomas R. Marsh,[8] James Munday,[8,9] Ingrid Pelisoli,[8] David I. Sahman,[1] James F. Wild,[1]
[1]*Department of Physics and Astronomy, Hicks Building, The University of Sheffield, Sheffield, S3 7RH, UK*
[2]*Anton Pannekoek Institute for Astronomy, University of Amsterdam, 1090 GE Amsterdam, The Netherlands*
[3]*Departament de Física, Universitat Politècnica de Catalunya, c/Esteve Terrades 5, 08860 Castelldefels, Spain*
[4]*Institut d'Estudis Espacials de Catalunya, Ed. Nexus-201, c/Gran Capità 2-4, 08034 Barcelona, Spain*
[5]*Institute of Astronomy, University of Cambridge, Madingley Road, Cambridge CB3 0HA, UK*
[6] *Instituto de Astrofisica de Canarias, E38205 La Laguna, Tenerife, Spain*
[7]*Department of Astrophysics, School of Physics and Astronomy, Tel Aviv University, Tel Aviv 6997801, Israel*
[8]*Department of Physics, University of Warwick, Gibbet Hill Road, Coventry, CV4 7AL, UK*
[9]*Isaac Newton Group of Telescopes, Apartado de Correos 368, E-38700 Santa Cruz de La Palma, Spain*

Accepted XXX. Received YYY; in original form ZZZ

ABSTRACT

Wide-field time-domain photometric sky surveys are now finding hundreds of eclipsing white dwarf plus M dwarf binaries, a population encompassing a wealth of information and potential insight into white dwarf and close binary astrophysics. Precise follow-up observations are essential in order to fully constrain these systems and capitalise on the power of this sample. We present the first results from our program of high-speed, multi-band photometric follow-up. We develop a method to measure temperatures, (model-dependent) masses, and radii for both components from the eclipse photometry alone and characterize 34 white dwarf binaries, finding general agreement with independent estimates using an alternative approach while achieving around a factor of two increase in parameter precision. In addition to these parameter estimates, we discover a number of interesting systems – finding four with sub-stellar secondaries, doubling the number of eclipsing examples, and at least six where we find the white dwarf to be strongly magnetic, making these the first eclipsing examples of such systems and key to investigating the mechanism of magnetic field generation in white dwarfs. We also discover the first two pulsating white dwarfs in detached and eclipsing post-common-envelope binaries – one with a low-mass, likely helium core, and one with a relatively high mass, towards the upper end of the known sample of ZZ Cetis. Our results demonstrate the power of eclipse photometry, not only as a method of characterising the population, but as a way of discovering important systems that would have otherwise been missed by spectroscopic follow-up.

Key words: (stars:) binaries: eclipsing – (stars:) white dwarfs – stars: late-type – techniques: photometric

1 INTRODUCTION

A significant fraction of field stars are formed as part of a binary system (Eggleton & Tokovinin 2008; Raghavan et al. 2010). Of these binaries, around 25 per cent are formed with sufficiently small orbital separations such that at some stage in their lives the two stars will interact with each other (Willems & Kolb 2004), transferring material between them and affecting their future evolution. For many of these interacting systems, the mass-transfer will lead to a common-envelope phase, initiated by the post-main-sequence evolution of the more massive star (the primary). This involves both stars being engulfed by the expanding outer envelope of the more massive star, with the resulting drag forces causing the hot core of the primary star and its main-sequence companion to spiral in to small orbital separations and therefore short orbital periods ranging from hours to a few days. The lost orbital energy and angular momentum from the binary is imparted into the envelope, ejecting it (Paczynski 1976), where it may then be ionised and lit up by the hot remnant core, appearing as a planetary nebula for a period of time (Jones & Boffin 2017) before the core cools and stratifies to become a white dwarf (WD). As well as being a key tracer of the common-envelope phase, these short period detached post-common-envelope binaries (PCEBs) made up of a WD and a main-sequence star are the progenitors to many of the most interesting and exotic astrophysical objects and phenomena in the Universe, including the cosmologically important type Ia supernovae.

Binaries made up of a WD and a main-sequence star are typically split into two categories, one of which containing the WDs

★ E-mail: ajbrown2@sheffield.ac.uk (AJB)

with solar-type companions (WD+FGK) and the other made up of WDs with companions of spectral type M and later (referred to as WD+dM). These categories reflect the differences in observational properties, with the WD+dM binaries being relatively easy to find due to the two stars often contributing a similar amount of flux at optical wavelengths. This has allowed a large sample to be extracted from spectroscopic surveys (Rebassa-Mansergas et al. 2007, 2010, 2012, 2016), making them the most common for many years. More recently, WD+FGK binaries have been found by using UV excesses to discern systems with WDs that would otherwise be outshone by their companion at optical wavelengths (Parsons et al. 2016; Rebassa-Mansergas et al. 2017).

While both types can be found with short orbital periods (Hernandez et al. 2022) – and therefore with small orbital separations with a relatively high chance of eclipse – the advantage of the WD+dM PCEBs is that the WD contributes enough of the total flux such that the eclipses can be detected, enabling them to be found in photometric surveys (Parsons et al. 2013, 2015). Eclipsing systems are a gold standard in astrophysics, allowing for incredibly precise measurements of the stellar and binary parameters, with typical precisions at or below the percent level. The result of this is that eclipsing PCEBs are some of the best laboratories of stellar and binary physics available to us and, as such, have been used to test and study a multitude of effects including, but not limited to: precisely measuring mass-radius relations of WDs (Parsons et al. 2017b), confirming the over-inflation of M dwarfs relative to theoretical models (Parsons et al. 2018), distinguishing the transition between helium and carbon-oxygen core compositions in WDs (Parsons et al. 2017b), finding systems with brown dwarf companions (Beuermann et al. 2013; Parsons et al. 2017a; Casewell et al. 2020a; van Roestel et al. 2021), and identifying unusual systems such as merger products and extremely low metallicity systems (O'Brien et al. 2001; Rebassa-Mansergas et al. 2019).

In the current era of wide-field time-domain photometric sky surveys, such as the Zwicky Transient Facility (ZTF; Masci et al. 2019; Bellm et al. 2019; Graham et al. 2019), the number of known eclipsing PCEBs is increasing drastically, with ZTF alone contributing to more than an order of magnitude increase (van Roestel et al. in prep), so far, on the previously known sample (Parsons et al. 2015). The Legacy Survey of Space and Time (LSST; Ivezić et al. 2019) carried out by the Vera Rubin Observatory in the near future will only accelerate this increase. Follow-up of this vast quantity of systems will be an ongoing challenge, particularly as many of these will be extremely faint, but they will provide much-needed insight into the relatively uncertain physics of the common-envelope as well as uncovering rare systems that may have implications for specific areas of stellar or binary physics. These include, but are not limited to, systems containing magnetic, pulsating, or high-mass WDs, as well as those with brown dwarf companions.

Previous work has shown that high-cadence multi-colour photometric observations of the primary eclipse is enough to accurately and efficiently characterize detached eclipsing PCEBs (Brown et al. 2022). This method makes use of the eclipse to cleanly disentangle the spectral energy distributions of the two components and constrains the effective temperatures, while using the shape of the eclipse to measure the orbital inclination and the stellar radii. These, in turn, provide information about the stellar masses through the use of mass-radius relations. A photometric method such as this is especially important as fainter systems are discovered – particularly in the LSST era – making spectroscopic follow-up even more difficult, and in many cases, impractical. With this in mind, we have undertaken a program of high-cadence photometric follow-up of eclipsing WD+dM PCEBs (first discovered by van Roestel et al. (in prep)) with the goal of characterizing a significant fraction and discovering a number of rare systems among them. Here we present the first results of this follow-up.

2 OBSERVATIONS

2.1 Target selection

Our targets for follow-up were selected from the detached eclipsing WD+dM systems discovered by van Roestel et al. (in prep) using data from ZTF. In brief, this sample was created by searching for periodic outliers in the ZTF photometry, indicative of eclipses. The primary biases are therefore related to the probability of a given system eclipsing as viewed from Earth and the ability to detect an eclipse within the ZTF data. The former is dominated by the orbital period (with a very weak dependence on the secondary radius), while the latter is dominated by the signal-to-noise ratio of the eclipse, with a heavy dependence on the depth of the eclipse (and a much weaker dependence on the duration of the eclipse). A more detailed description of the full ZTF eclipsing WD+dM sample identification method and the biases within it will be presented in van Roestel et al. (in prep).

We restricted our target list to systems visible from the La Silla Observatory (Dec < +25 deg) and brighter than $g = 19.5$ mag. We typically observed systems with eclipse timings that made for the most efficient use of telescope time on a particular night however we also tried to prioritise systems with longer periods where possible since the eclipses of these systems are more difficult to observe. Systems with ZTF light curves that indicated they may be of particular interest were also prioritised. This includes systems with in-eclipse flux measurements at or below the detection threshold of ZTF (indicative of brown dwarf companions) and systems with unusual ZTF light curves, showing variability inconsistent with typical binary variability mechanisms and indicating the presence of a magnetic WD.

A journal of observations is included in Table A1.

2.2 High speed photometry

Our photometric follow-up observations made use of the three-band frame-transfer camera, ULTRACAM (Dhillon et al. 2007), mounted on the 3.6 m New Technology Telescope (NTT) at the ESO La Silla Observatory in Chile, to obtain high-cadence multi-colour photometry of the primary eclipse of each system – the eclipse of the WD by its companion. For all targets observed with ULTRACAM we used the higher throughput Super-SDSS $u_s\, g_s\, i_s$ filters (Dhillon et al. 2021), with the exception of one observation where the r_s filter was used in place of i_s. For a few of the systems thought to harbour magnetic WDs, we obtained high-speed photometry with the quintuple band frame-transfer camera, HiPERCAM (Dhillon et al. 2021), mounted on the 10.4 m Gran Telescopio Canarías (GTC) at the Roque de los Muchachos observatory in La Palma, again equipped with Super-SDSS $u_s\, g_s\, r_s\, i_s\, z_s$ filters.

All observations were bias-subtracted and flat-field corrected (and fringe corrected in the case of the HiPERCAM z_s band) using the HiPERCAM pipeline[1]. Differential aperture photometry was then extracted using a variable aperture radius set to scale with the measured full width at half-maximum (FWHM) in each frame in order to

[1] https://github.com/HiPERCAM/hipercam

remove effects due to seeing and transparency variations. For this we use a target aperture radius of $1.8 \times FWHM$. In observations with lower signal-to-noise ratios, optimal extraction (Naylor 1998) was also performed, with the extraction method resulting in the highest signal-to-noise light curve being the one that was used.

Flux calibration was then performed by fitting the atmospheric extinction in each band using one or more observing runs taken on the same night as the target observations (each spanning a minimum of 0.2 airmasses). The atmospheric extinction measurements were combined with an observation of an ULTRACAM flux standard star (see Brown et al. 2022, table A3), reduced using a larger target aperture radius of $2.5 \times FWHM$, in order to measure the instrumental zeropoint for the night. The calibrated flux of the comparison star was then determined using the same target aperture radius as for the flux standard star, which was then used to flux calibrate the target. When using optimally extracted photometry, the flux calibration was still performed on the data reduced using a standard aperture photometry extraction. This calibration was then applied to the optimally extracted photometry to prevent systematic absolute flux errors between the two methods. These flux calibration steps were performed using the CAM_CAL[2] package.

3 METHOD

We fit the flux calibrated eclipse photometry using the PYLCURVE[3] package, a python wrapper for LCURVE's LROCHE routine (Copperwheat et al. 2010). In general, we follow the method of Brown et al. (2022) which involves fitting the eclipse photometry in multiple filters simultaneously with eight free parameters. These are the effective temperatures, T_1 and T_2, which define the spectral energy distributions (SEDs) of both stars through the use of stellar atmosphere models (Claret et al. 2020; Husser et al. 2013); the stellar masses, M_1 and M_2; the binary inclination, i; the parallax, ϖ; the interstellar reddening, $E(B-V)$; and the time of mid-eclipse, T_0. With the use of mass-radius relations and a given (fixed) orbital period, P, the radii of both stars and the orbital separation of the binary can be defined allowing model light curves to be generated for each filter. See Brown et al. (2022) for more details on this method.

For this work, however, we implement two changes to the methodology mentioned above, both regarding the spectral modelling of the secondary star:

(i) Previously, PHOENIX stellar atmospheres (Husser et al. 2013) were used to model the SED of the secondary star (Brown et al. 2022). However, these models are limited to a minimum effective temperature of 2300 K, preventing the modelling of systems with brown dwarf companions. We have therefore switched to using the BT-Settl CIFIST stellar atmosphere grid (Allard et al. 2012) which go as low as 1200 K, allowing for a seamless transition to the brown dwarf regime and keeping our modelling consistent throughout.

(ii) It is well known that there are significant differences in the synthetic photometry of low mass stars calculated using different spectral models for a given effective temperature and surface gravity. This is most apparent for lower effective temperatures (<3500 K), with models struggling to reproduce the transitions from M dwarfs to L dwarfs to T dwarfs (Saumon & Marley 2008; Allard et al. 2012; Best et al. 2021). Rigidly defining the SED of the secondary from these spectral models could therefore introduce problems where the model photometry cannot reproduce the observed SED of the star in question to the precision of our observations. We counter this by allowing the secondary to have a separate effective temperature in each observed bandpass. Despite being allowed to vary, these individual filter-specific effective temperatures should be consistent with each other at a certain level. We implement this consistency requirement using priors to favour solutions where these effective temperatures are similar across the different filters.

In order to inform the priors on the filter-specific secondary temperatures mentioned in item (ii), we use a sample of 15 279 well-characterised M dwarfs (Morrell & Naylor 2019). Cross-matching this sample with SDSS DR13 returns a sample of 5 222 M dwarfs, on which we then make colour cuts informed by synthetic photometry of the BT-SETTL-CIFIST model atmospheres ($4.0 < (u'-i') < 6.4$ and $1.5 < (g'-i') < 3.4$) to remove many of the extreme outliers. This leaves 4 158 M dwarfs with SDSS photometry. We then fit fifth-order polynomials to the measured effective temperature as a function of $u'-i'$ and $g'-i'$ colours individually, using an iterative sigma clipping procedure with a 3σ cut to remove any outliers that remain after the initial colour cuts (Figure 1). The standard deviations of the residuals of the remaining points are 80 K for a $u'-i'$ colour and 30 K for a $g'-i'$ colour. We therefore implement Gaussian priors on the difference in effective temperature between the u' and i', and g' and i' bands of 80 K and 30 K respectively, both centred at zero. As, with this method, there are as many temperature measurements available for the secondary as filters used, we take the i_s-band measurement as being representative of the true secondary temperature. We make this choice based on it being the the band where the secondary is brightest and is therefore the most strongly constrained by the photometry.

As in Brown et al. (2022), we use a Markov Chain Monte Carlo (MCMC) method to fit each light curve, implemented through the PYTHON package, EMCEE[4] (Foreman-Mackey et al. 2013). We run each fit for a minimum of 10 000 steps using 100 walkers and inspect each fit manually for convergence and stability. Each system is first fit using a carbon-oxygen (CO) core WD mass-radius relation (Bédard et al. 2020; Blouin et al. 2018; Tremblay et al. 2011) with the fit then being repeated using a helium (He) core model (Panei et al. 2007) if the best-fit CO-core WD mass is below 0.5 $M_\odot$. If this subsequent fit using the He-core model is restricted by the upper mass limit of the He-core models – 0.5 $M_\odot$ – then we consider the WD to have a CO core-composition, if not then we assume the WD to possess a He core.

4 RESULTS

The results of our light curve fits are presented in Table 1 and Table 2 – note that of the 43 systems that we have followed-up, 9 do not have measured parameters because they either harbour magnetic WDs or are strong candidates (see section 5.4). Our best-fit values are taken to be the median of the posterior distributions of the MCMC with lower and upper uncertainties taken as the 16th and 84th percentiles respectively. As in Brown et al. (2022), the formal uncertainties from the MCMC do not include contributions from systematic errors and so we attempt to take this into account by adding estimated systematic uncertainties in quadrature with the formal uncertainties of the MCMC. We add 1.5 per cent in quadrature with the uncertainties on the primary temperature (Gianninas et al. 2011), T_1, and

[2] https://github.com/Alex-J-Brown/cam_cal
[3] https://github.com/Alex-J-Brown/pylcurve
[4] https://emcee.readthedocs.io/en/stable/

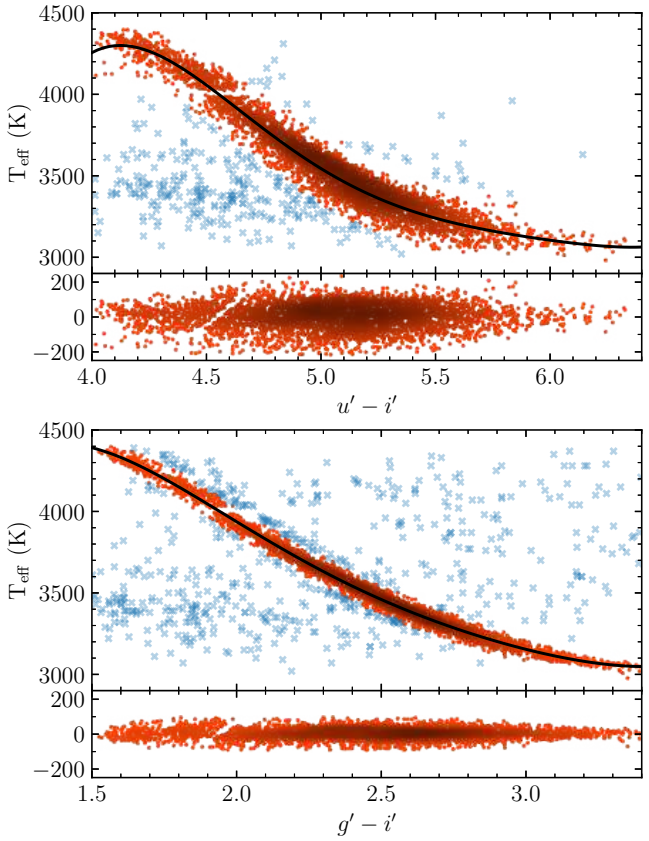

Figure 1. Effective temperatures of M dwarfs measured by Morrell & Naylor (2019) against their SDSS colours. Blue crosses show points discarded by the sigma clipping procedure and the solid black lines show the final polynomial fits to these sigma-clipped distributions. The residuals of these fits, from which we calculate the standard deviations, are shown in the panels below. The gap in the sample at an effective temperature of 4000 K is due to a discontinuity in the model grid used by Morrell & Naylor (2019).

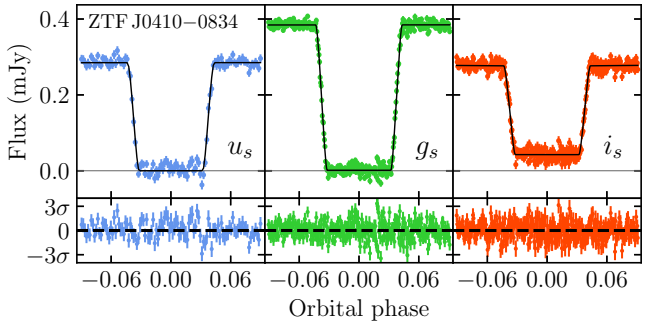

Figure 2. ULTRACAM $u_s\, g_s\, i_s$ eclipse light curve (coloured points) of ZTF J041016.82−083419.5 with the best-fit light curve model over-plotted in black and the residuals of this fit shown below. The zero-flux level is shown by the horizontal grey line.

100 K in quadrature with the secondary temperature, T_2. We also add 1 per cent in quadrature with the WD mass, M_1, and 5 per cent in quadrature with the secondary mass, M_2 (for the reasons explained in Brown et al. (2022)). These contributions are included in the uncertainties shown in Table 1 and in all figures. An example ULTRACAM eclipse light curve and best-fit model is shown in Figure 2 with all best-fit light curves shown in Appendix B.

5 DISCUSSION

5.1 Comparison with previous parameters

Initial parameter estimates for these systems were made by fitting the ZTF time-series photometry alongside photometric measurements from other surveys, where available, covering a wide wavelength range (van Roestel et al. in prep). Comparing our parameters determined from the three-band eclipse photometry against these initial estimates demonstrates general agreement between the two methods (Figure 3). The WD temperatures, in particular, show excellent agreement but there are some significant differences in the measured masses for certain systems. This may be due, in part, to the survey SED data used by van Roestel et al. (in prep) being taken at a range of different orbital phases and therefore suffering from increased systematics due to ellipsoidal modulation or reflection effect. As the method we have used in this work has previously been shown to retrieve accurate parameters (Brown et al. 2022), this may imply a slight underestimation in the uncertainties determined by combining SED fitting with ZTF photometry. The parameters determined using the high-speed eclipse photometry are typically more precise than those measured by van Roestel et al. (in prep). This is most apparent for the primary and secondary masses with a median uncertainty in the WD mass from the ULTRACAM photometry of 2.6 per cent, and 7.2 per cent for the secondary mass. These values are 6.0 per cent and 13.7 per cent respectively from the ZTF photometry for the same systems and so the ULTRACAM measurements are typically a factor of 2 more precise. This is likely due to the high time resolution of the ULTRACAM photometry, enabling the duration of the eclipse as well as the ingress and egress to be measured very precisely.

In addition to the initial parameter estimates discussed above, two of the systems fit in this work have been included in previously published analyses – ZTF J125620.57+211725.8 and ZTF J164441.18+243428.2. Comparisons with these previous works are made below.

5.1.1 ZTF J125620.57+211725.8

ZTF J125620.57+211725.8 was previously fitted by Rebassa-Mansergas et al. (2021), using the Virtual Observatory SED Analyser (VOSA) to fit the available survey photometry. Out of the 112 systems that they analysed, 13 systems were determined to possess a WD with a mass below 0.2 $M_\odot$. It is not known how such low mass WDs could form in PCEBs with low-mass main sequence companions – with any mass transfer initiating a common envelope phase in which the envelope would most likely not gain sufficient energy to be ejected, leading to a merger scenario (Rebassa-Mansergas et al. 2021). This system is – as far as we know – the only one of these 13 systems that eclipses, enabling a valuable check on the system parameters. Our fit to the eclipse photometry determines the WD mass to be 0.48 ± 0.01 $M_\odot$, discrepant with the 0.155 ± 0.02 $M_\odot$ obtained from VOSA by over 14σ. We encourage spectroscopic follow-up of this system in order to determine the cause of this large discrepancy and the true WD mass.

Table 1. Best fit stellar parameters to the ULTRACAM eclipse photometry. Uncertainties include estimated systematic errors added in quadrature with the formal uncertainties of the MCMC. These estimated systematics are 1.5 per cent on T_1 (Gianninas et al. 2011), 100 K on T_2, 1 per cent for M_1, and 5 per cent for M_2 (Brown et al. 2022).

Target	He/CO	T_1 (K)	M_1 ($M_\odot$)	R_1 ($R_\odot$)	$\log(g_1)$	T_2 (K)	M_2 ($M_\odot$)	R_2 ($R_\odot$)	R_2/R_{L1}
ZTF J041016.82−083419.5	He	14690^{+560}_{-550}	$0.355^{+0.015}_{-0.011}$	$0.0204^{+0.0004}_{-0.0006}$	$7.37^{+0.04}_{-0.03}$	2840^{+110}_{-110}	$0.123^{+0.009}_{-0.008}$	$0.151^{+0.008}_{-0.006}$	$0.680^{+0.033}_{-0.021}$
ZTF J051902.06+092526.4	He	10750^{+770}_{-580}	$0.391^{+0.019}_{-0.029}$	$0.0178^{+0.0009}_{-0.0005}$	$7.53^{+0.04}_{-0.08}$	2800^{+140}_{-110}	$0.177^{+0.014}_{-0.019}$	$0.214^{+0.012}_{-0.018}$	$0.842^{+0.079}_{-0.084}$
ZTF J052848.24+215629.0	CO	12100^{+700}_{-630}	$0.787^{+0.025}_{-0.025}$	$0.0105^{+0.0003}_{-0.0003}$	$8.29^{+0.04}_{-0.04}$	3130^{+110}_{-110}	$0.184^{+0.014}_{-0.013}$	$0.220^{+0.011}_{-0.009}$	$0.408^{+0.014}_{-0.011}$
ZTF J053708.26−245014.6	He	16100^{+440}_{-410}	$0.397^{+0.009}_{-0.007}$	$0.0191^{+0.0002}_{-0.0002}$	$7.48^{+0.02}_{-0.02}$	2970^{+100}_{-100}	$0.204^{+0.012}_{-0.011}$	$0.241^{+0.007}_{-0.005}$	$0.333^{+0.006}_{-0.004}$
ZTF J061530.96+051041.8	CO	15220^{+600}_{-510}	$0.560^{+0.011}_{-0.011}$	$0.0139^{+0.0002}_{-0.0002}$	$7.90^{+0.02}_{-0.02}$	3380^{+110}_{-110}	$0.533^{+0.030}_{-0.029}$	$0.547^{+0.013}_{-0.011}$	$0.531^{+0.008}_{-0.008}$
ZTF J063808.71+091027.4	CO	22500^{+1200}_{-1000}	$0.604^{+0.013}_{-0.011}$	$0.0136^{+0.0001}_{-0.0002}$	$7.95^{+0.02}_{-0.02}$	3320^{+110}_{-110}	$0.410^{+0.024}_{-0.022}$	$0.432^{+0.012}_{-0.008}$	$0.295^{+0.005}_{-0.004}$
ZTF J063954.70+191958.0	CO	15980^{+520}_{-520}	$0.701^{+0.011}_{-0.009}$	$0.0117^{+0.0001}_{-0.0001}$	$8.15^{+0.01}_{-0.01}$	3200^{+100}_{-100}	$0.210^{+0.011}_{-0.011}$	$0.246^{+0.004}_{-0.002}$	$0.398^{+0.004}_{-0.002}$
ZTF J064242.41+131427.6	CO	14560^{+540}_{-500}	$0.633^{+0.011}_{-0.008}$	$0.0127^{+0.0001}_{-0.0001}$	$8.03^{+0.02}_{-0.01}$	3110^{+100}_{-100}	$0.150^{+0.008}_{-0.008}$	$0.183^{+0.004}_{-0.001}$	$0.438^{+0.006}_{-0.002}$
ZTF J065103.70+145246.2	CO	13140^{+560}_{-670}	$0.515^{+0.019}_{-0.020}$	$0.0145^{+0.0003}_{-0.0003}$	$7.83^{+0.03}_{-0.04}$	3170^{+120}_{-110}	$0.242^{+0.018}_{-0.019}$	$0.276^{+0.012}_{-0.013}$	$0.589^{+0.018}_{-0.019}$
ZTF J070458.08−020103.3	CO	9280^{+230}_{-250}	$0.500^{+0.012}_{-0.015}$	$0.0143^{+0.0003}_{-0.0002}$	$7.82^{+0.02}_{-0.03}$	3300^{+100}_{-100}	$0.344^{+0.018}_{-0.020}$	$0.370^{+0.006}_{-0.010}$	$0.915^{+0.040}_{-0.043}$
ZTF J071759.04+113630.2	CO	21110^{+920}_{-750}	$0.528^{+0.016}_{-0.017}$	$0.0149^{+0.0003}_{-0.0003}$	$7.81^{+0.03}_{-0.03}$	3150^{+120}_{-110}	$0.296^{+0.020}_{-0.022}$	$0.326^{+0.013}_{-0.015}$	$0.320^{+0.008}_{-0.009}$
ZTF J071843.68−085232.1	CO	18940^{+870}_{-880}	$0.794^{+0.019}_{-0.018}$	$0.0106^{+0.0002}_{-0.0002}$	$8.28^{+0.03}_{-0.03}$	3120^{+110}_{-110}	$0.306^{+0.020}_{-0.019}$	$0.335^{+0.012}_{-0.011}$	$0.555^{+0.014}_{-0.012}$
ZTF J080441.95−021545.7	CO	13430^{+560}_{-550}	$0.577^{+0.010}_{-0.009}$	$0.0134^{+0.0001}_{-0.0001}$	$7.94^{+0.01}_{-0.01}$	$< 1510^{+260}_{-200}$	$< 0.069^{+0.007}_{-0.007}$	$0.098^{+0.002}_{-0.001}$	$0.377^{+0.008}_{-0.006}$
ZTF J080542.98−143036.3	He	26500^{+1200}_{-9000}	$0.393^{+0.013}_{-0.013}$	$0.0239^{+0.0007}_{-0.0006}$	$7.28^{+0.03}_{-0.04}$	3250^{+120}_{-110}	$0.291^{+0.020}_{-0.023}$	$0.331^{+0.013}_{-0.017}$	$0.586^{+0.016}_{-0.021}$
ZTF J094826.35+253810.6	CO	11290^{+480}_{-450}	$0.504^{+0.026}_{-0.024}$	$0.0145^{+0.0004}_{-0.0004}$	$7.82^{+0.05}_{-0.05}$	3120^{+120}_{-120}	$0.169^{+0.015}_{-0.014}$	$0.205^{+0.013}_{-0.012}$	$0.546^{+0.024}_{-0.024}$
ZTF J102254.00−080327.3	CO	8330^{+260}_{-250}	$0.605^{+0.027}_{-0.025}$	$0.0127^{+0.0003}_{-0.0003}$	$8.01^{+0.04}_{-0.04}$	3170^{+110}_{-110}	$0.405^{+0.030}_{-0.029}$	$0.428^{+0.021}_{-0.020}$	$0.620^{+0.023}_{-0.021}$
ZTF J102653.47−101330.3	He	19320^{+710}_{-670}	$0.376^{+0.012}_{-0.010}$	$0.0214^{+0.0004}_{-0.0007}$	$7.35^{+0.04}_{-0.02}$	2840^{+110}_{-110}	$0.105^{+0.008}_{-0.006}$	$0.134^{+0.007}_{-0.004}$	$0.558^{+0.021}_{-0.012}$
ZTF J103448.82+005201.9	He	10060^{+410}_{-370}	$0.455^{+0.007}_{-0.007}$	$0.0159^{+0.0001}_{-0.0001}$	$7.69^{+0.01}_{-0.01}$	$< 1550^{+250}_{-230}$	$< 0.067^{+0.005}_{-0.006}$	$0.097^{+0.001}_{-0.001}$	$0.460^{+0.010}_{-0.008}$
ZTF J104906.96−175530.7	He	13000^{+440}_{-460}	$0.426^{+0.010}_{-0.007}$	$0.0173^{+0.0001}_{-0.0002}$	$7.59^{+0.02}_{-0.01}$	3170^{+100}_{-110}	$0.198^{+0.012}_{-0.010}$	$0.235^{+0.007}_{-0.003}$	$0.402^{+0.008}_{-0.003}$
ZTF J122009.98+082155.0	CO	10170^{+270}_{-260}	$0.580^{+0.017}_{-0.018}$	$0.0132^{+0.0003}_{-0.0002}$	$7.96^{+0.03}_{-0.03}$	3140^{+110}_{-110}	$0.275^{+0.019}_{-0.020}$	$0.306^{+0.012}_{-0.013}$	$0.157^{+0.004}_{-0.004}$
ZTF J125620.57+211725.8	CO	5073^{+79}_{-79}	$0.479^{+0.010}_{-0.009}$	$0.0141^{+0.0001}_{-0.0001}$	$7.82^{+0.02}_{-0.01}$	2950^{+100}_{-100}	$0.101^{+0.005}_{-0.005}$	$0.125^{+0.001}_{-0.001}$	$0.152^{+0.001}_{-0.001}$
ZTF J130228.34−003200.2	CO	11790^{+400}_{-330}	$0.811^{+0.021}_{-0.016}$	$0.0102^{+0.0002}_{-0.0002}$	$8.33^{+0.03}_{-0.02}$	3030^{+100}_{-100}	$0.179^{+0.012}_{-0.010}$	$0.216^{+0.008}_{-0.005}$	$0.502^{+0.013}_{-0.009}$
ZTF J134151.70−062613.9	CO	58300^{+8400}_{-8700}	$0.509^{+0.038}_{-0.035}$	$0.0225^{+0.0009}_{-0.0016}$	$7.43^{+0.09}_{-0.04}$	2800^{+210}_{-220}	$0.126^{+0.015}_{-0.009}$	$0.159^{+0.018}_{-0.007}$	$0.617^{+0.062}_{-0.021}$
ZTF J140036.65+081447.4	CO	13340^{+650}_{-610}	$0.563^{+0.009}_{-0.008}$	$0.0137^{+0.0001}_{-0.0001}$	$7.92^{+0.01}_{-0.01}$	2970^{+100}_{-100}	$0.232^{+0.012}_{-0.012}$	$0.268^{+0.003}_{-0.001}$	$0.418^{+0.003}_{-0.001}$
ZTF J140423.86+065557.7	CO	14980^{+470}_{-460}	$0.736^{+0.016}_{-0.015}$	$0.0113^{+0.0002}_{-0.0002}$	$8.20^{+0.02}_{-0.02}$	3100^{+100}_{-100}	$0.409^{+0.023}_{-0.023}$	$0.432^{+0.010}_{-0.010}$	$0.884^{+0.045}_{-0.031}$
ZTF J140537.34+103919.0	He	29900^{+9000}_{-1100}	$0.404^{+0.008}_{-0.008}$	$0.0279^{+0.0006}_{-0.0006}$	$7.15^{+0.02}_{-0.02}$	3430^{+130}_{-140}	$0.085^{+0.005}_{-0.005}$	$0.112^{+0.003}_{-0.003}$	$0.234^{+0.004}_{-0.004}$
ZTF J140702.57+211559.7	He	10870^{+350}_{-350}	$0.406^{+0.018}_{-0.014}$	$0.0173^{+0.0004}_{-0.0004}$	$7.57^{+0.04}_{-0.03}$	3160^{+110}_{-110}	$0.263^{+0.021}_{-0.016}$	$0.296^{+0.015}_{-0.009}$	$0.702^{+0.029}_{-0.016}$
ZTF J145819.54+131326.7	CO	9420^{+260}_{-260}	$0.581^{+0.010}_{-0.010}$	$0.0131^{+0.0001}_{-0.0001}$	$7.97^{+0.01}_{-0.01}$	$< 1730^{+240}_{-270}$	$< 0.067^{+0.006}_{-0.006}$	$0.095^{+0.001}_{-0.000}$	$0.446^{+0.011}_{-0.006}$
ZTF J162644.18−101854.3	CO	36700^{+2700}_{-2700}	$0.499^{+0.015}_{-0.012}$	$0.0180^{+0.0002}_{-0.0003}$	$7.62^{+0.02}_{-0.01}$	3180^{+110}_{-110}	$0.212^{+0.013}_{-0.011}$	$0.259^{+0.008}_{-0.003}$	$0.425^{+0.008}_{-0.004}$
ZTF J163421.00−271321.7	He	10680^{+790}_{-630}	$0.436^{+0.042}_{-0.054}$	$0.0166^{+0.0013}_{-0.0009}$	$7.64^{+0.09}_{-0.12}$	2400^{+130}_{-120}	$0.134^{+0.016}_{-0.020}$	$0.163^{+0.019}_{-0.022}$	$0.759^{+0.128}_{-0.099}$
ZTF J164441.18+243428.2	He	13270^{+520}_{-460}	$0.382^{+0.020}_{-0.018}$	$0.0188^{+0.0007}_{-0.0007}$	$7.47^{+0.05}_{-0.05}$	2500^{+110}_{-110}	$0.103^{+0.009}_{-0.009}$	$0.129^{+0.009}_{-0.008}$	$0.607^{+0.033}_{-0.028}$
ZTF J180256.45−005458.3	He	10770^{+630}_{-500}	$0.458^{+0.019}_{-0.021}$	$0.0160^{+0.0004}_{-0.0003}$	$7.69^{+0.03}_{-0.04}$	3150^{+110}_{-110}	$0.150^{+0.010}_{-0.011}$	$0.182^{+0.008}_{-0.010}$	$0.319^{+0.010}_{-0.012}$
ZTF J182848.77+230838.0	CO	16620^{+560}_{-650}	$0.594^{+0.009}_{-0.008}$	$0.0134^{+0.0001}_{-0.0001}$	$7.96^{+0.01}_{-0.01}$	$< 2290^{+110}_{-120}$	$< 0.068^{+0.007}_{-0.006}$	$0.096^{+0.002}_{-0.000}$	$0.392^{+0.009}_{-0.005}$
ZTF J195456.71+101937.5	CO	21500^{+1000}_{-1100}	$0.509^{+0.015}_{-0.012}$	$0.0154^{+0.0002}_{-0.0002}$	$7.77^{+0.03}_{-0.02}$	3480^{+110}_{-110}	$0.449^{+0.028}_{-0.026}$	$0.470^{+0.016}_{-0.013}$	$0.523^{+0.012}_{-0.010}$

5.1.2 ZTF J164441.18+243428.2

ZTF J164441.18+243428.2 was one of the four deeply eclipsing PCEBs found and fitted by Kosakowski et al. (2022). For this target in particular they did not detect the eclipse minimum and so their parameters from the light curve fit represent limits rather than specific values. As would be expected, our light curve fit to the ULTRACAM photometry is consistent with these parameter limits. As well as fitting the eclipse light curve Kosakowski et al. (2022) performed a spectroscopic fit to the WD, determining the effective temperature, surface gravity, and mass (determined from the surface gravity using CO-core composition models). From our fit to the ULTRACAM photometry we find an effective temperature of 13270 ± 490 K, cooler than the 14900 ± 760 K determined by their spectroscopic fit but still consistent to within 2σ. For the WD mass there is a little more deviation, with our fit finding a WD mass of 0.38 ± 0.02 $M_\odot$, 2.3σ below the 0.55 ± 0.07 $M_\odot$ found from their spectroscopic fit and suggesting a He-core composition rather than a CO-core. For the companion, Kosakowski et al. (2022) estimate a mass of 0.084 ± 0.004 $M_\odot$ by fitting the Pan-STARRS SED with a composite model, placing it close to the hydrogen-burning limit. We find a higher mass of 0.103 ± 0.009 $M_\odot$ from our light curve fit taking it into more typically stellar territory. Again though, these two values are consistent to within 2σ. Overall, our fit to the ULTRACAM photometry is fully consistent with their light curve fit and consistent with their spectroscopic and Pan-STARRS SED fits at around the 2σ level.

Table 2. Best fit binary parameters to the ULTRACAM eclipse photometry. The orbital periods are listed here for reference but are not fitted parameters and so do not have corresponding uncertainties. The *Gaia* DR3 parallax measurements are included for comparison.

Target	i(°)	a ($R_\odot$)	$E(B-V)$	$\varpi_{\rm UCAM}$	$\varpi_{\rm Gaia}$	T_0 (BMJD(TDB))	P (d)
ZTF J041016.82−083419.5	$86.6^{+2.1}_{-1.7}$	$0.616^{+0.009}_{-0.006}$	$0.031^{+0.017}_{-0.017}$	$3.863^{+0.091}_{-0.078}$	4.07 ± 0.11	59646.0489782(16)	0.0811093
ZTF J051902.06+092526.4	$76.3^{+1.1}_{-0.6}$	$0.715^{+0.012}_{-0.020}$	$0.112^{+0.028}_{-0.023}$	$2.835^{+0.140}_{-0.140}$	2.92 ± 0.30	59251.0519387(57)	0.0929131
ZTF J052848.24+215629.0	$87.7^{+1.4}_{-1.0}$	$1.546^{+0.017}_{-0.016}$	$0.090^{+0.020}_{-0.021}$	$5.666^{+0.104}_{-0.111}$	5.59 ± 0.13	59932.215321(52)	0.2259952
ZTF J053708.26−245014.6	$88.1^{+0.7}_{-0.6}$	$1.688^{+0.014}_{-0.010}$	$0.015^{+0.011}_{-0.010}$	$4.580^{+0.044}_{-0.047}$	4.574 ± 0.049	59251.2246115(52)	0.3277936
ZTF J061530.96+051041.8	$85.0^{+0.7}_{-0.7}$	$2.146^{+0.015}_{-0.014}$	$0.019^{+0.019}_{-0.013}$	$3.163^{+0.060}_{-0.051}$	3.166 ± 0.081	59280.12536567(83)	0.3481742
ZTF J063808.71+091027.4	$88.2^{+0.5}_{-0.6}$	$3.197^{+0.024}_{-0.019}$	$0.021^{+0.018}_{-0.015}$	$1.709^{+0.047}_{-0.047}$	1.65 ± 0.14	59252.1564861(10)	0.6576453
ZTF J063954.70+191958.0	$88.9^{+0.7}_{-0.7}$	$1.659^{+0.008}_{-0.005}$	$0.028^{+0.013}_{-0.015}$	$5.394^{+0.070}_{-0.075}$	5.387 ± 0.085	59251.17799186(52)	0.2593556
ZTF J064242.41+131427.6	$89.1^{+0.7}_{-0.8}$	$1.195^{+0.006}_{-0.003}$	$0.022^{+0.016}_{-0.013}$	$3.583^{+0.075}_{-0.073}$	3.77 ± 0.20	59252.10345653(59)	0.1710542
ZTF J065103.70+145246.2	$85.3^{+1.5}_{-1.0}$	$1.166^{+0.016}_{-0.017}$	$0.037^{+0.016}_{-0.018}$	$2.567^{+0.073}_{-0.076}$	2.70 ± 0.17	59252.2124933(16)	0.1677075
ZTF J070458.08−020103.3	$74.3^{+0.4}_{-0.2}$	$1.079^{+0.006}_{-0.010}$	$0.052^{+0.011}_{-0.013}$	$3.715^{+0.076}_{-0.075}$	3.643 ± 0.088	59253.2216462(43)	0.1413708
ZTF J071759.04+113630.2	$84.9^{+0.4}_{-0.3}$	$2.326^{+0.027}_{-0.030}$	$0.018^{+0.017}_{-0.012}$	$2.812^{+0.065}_{-0.072}$	2.74 ± 0.13	59251.1312794(93)	0.4527638
ZTF J071843.68−085232.1	$84.6^{+0.7}_{-0.7}$	$1.563^{+0.014}_{-0.013}$	$0.064^{+0.017}_{-0.019}$	$2.157^{+0.062}_{-0.058}$	2.39 ± 0.22	59283.1026109(12)	0.2158113
ZTF J080441.95−021545.7	$85.3^{+0.1}_{-0.1}$	$0.889^{+0.007}_{-0.004}$	$0.027^{+0.015}_{-0.014}$	$5.631^{+0.092}_{-0.089}$	5.47 ± 0.11	59646.09050723(97)	0.1209762
ZTF J080542.98−143036.3	$81.0^{+1.0}_{-0.7}$	$1.260^{+0.015}_{-0.019}$	$0.010^{+0.012}_{-0.008}$	$1.102^{+0.034}_{-0.039}$	1.39 ± 0.16	59646.18599526(74)	0.1981669
ZTF J094826.35+253810.6	$79.9^{+0.6}_{-0.6}$	$1.003^{+0.017}_{-0.017}$	$0.018^{+0.008}_{-0.009}$	$2.911^{+0.116}_{-0.108}$	2.94 ± 0.26	59239.2668295(95)	0.1418270
ZTF J102254.00−080327.3	$76.9^{+0.6}_{-0.6}$	$1.592^{+0.024}_{-0.023}$	$0.019^{+0.013}_{-0.012}$	$5.750^{+0.158}_{-0.160}$	5.58 ± 0.21	59280.2576703(43)	0.2314179
ZTF J102653.47−101330.3	$87.4^{+1.6}_{-1.5}$	$0.677^{+0.008}_{-0.006}$	$0.033^{+0.010}_{-0.010}$	$2.027^{+0.075}_{-0.063}$	1.65 ± 0.19	59237.2453759(14)	0.0929868
ZTF J103448.82+005201.9	$87.8^{+0.3}_{-0.2}$	$0.688^{+0.003}_{-0.003}$	$0.031^{+0.016}_{-0.015}$	$3.551^{+0.138}_{-0.138}$	3.20 ± 0.28	59253.2517553(11)	0.0915591
ZTF J104906.96−175530.7	$88.6^{+1.1}_{-1.1}$	$1.407^{+0.012}_{-0.006}$	$0.029^{+0.006}_{-0.008}$	$2.579^{+0.070}_{-0.070}$	2.47 ± 0.17	59238.3654607(11)	0.2447332
ZTF J122009.98+082155.0	$87.5^{+0.2}_{-0.2}$	$4.592^{+0.052}_{-0.056}$	$0.024^{+0.004}_{-0.008}$	$3.874^{+0.093}_{-0.106}$	3.53 ± 0.17	59252.2559984(25)	1.2329254
ZTF J125620.57+211725.8	$89.8^{+0.2}_{-0.2}$	$2.374^{+0.013}_{-0.012}$	$0.005^{+0.006}_{-0.004}$	$22.221^{+0.095}_{-0.094}$	22.171 ± 0.096	59641.3540758(33)	0.5560572
ZTF J130228.34−003200.2	$86.0^{+0.5}_{-0.6}$	$1.268^{+0.012}_{-0.008}$	$0.016^{+0.013}_{-0.011}$	$8.554^{+0.071}_{-0.068}$	8.555 ± 0.073	59252.387889(43)	0.1661310
ZTF J134151.70−062613.9	$86.8^{+2.4}_{-2.7}$	$0.764^{+0.018}_{-0.017}$	$0.030^{+0.009}_{-0.009}$	$0.894^{+0.089}_{-0.093}$	0.97 ± 0.12	59237.3073649(28)	0.0969505
ZTF J140036.65+081447.4	$89.2^{+0.6}_{-0.7}$	$1.589^{+0.006}_{-0.005}$	$0.005^{+0.008}_{-0.004}$	$2.155^{+0.070}_{-0.075}$	1.58 ± 0.30	59253.2966645(14)	0.2602766
ZTF J140423.86+065557.7	$84.5^{+1.0}_{-0.9}$	$1.342^{+0.010}_{-0.009}$	$0.025^{+0.007}_{-0.009}$	$2.538^{+0.059}_{-0.057}$	2.24 ± 0.14	59239.3665054(12)	0.1683096
ZTF J140537.34+103919.0	$88.5^{+0.4}_{-0.3}$	$1.389^{+0.009}_{-0.009}$	$0.016^{+0.010}_{-0.009}$	$0.752^{+0.031}_{-0.024}$	0.78 ± 0.26	59251.334651(12)	0.2714122
ZTF J140702.57+211559.7	$86.5^{+2.4}_{-2.0}$	$1.008^{+0.016}_{-0.011}$	$0.051^{+0.010}_{-0.013}$	$4.077^{+0.072}_{-0.070}$	4.079 ± 0.091	59643.3349542(63)	0.1432802
ZTF J145819.54+131326.7	$86.8^{+0.1}_{-0.2}$	$0.742^{+0.004}_{-0.003}$	$0.025^{+0.009}_{-0.012}$	$5.067^{+0.152}_{-0.154}$	4.86 ± 0.21	59252.3531663(17)	0.0920516
ZTF J162644.18−101854.3	$88.7^{+0.9}_{-1.1}$	$1.503^{+0.013}_{-0.010}$	$0.291^{+0.007}_{-0.013}$	$1.733^{+0.087}_{-0.085}$	1.91 ± 0.20	59253.3679108(15)	0.2530067
ZTF J163421.00−271321.7	$80.6^{+2.1}_{-1.5}$	$0.637^{+0.020}_{-0.028}$	$0.182^{+0.029}_{-0.026}$	$4.127^{+0.238}_{-0.230}$	4.24 ± 0.26	59253.3310632(36)	0.0780396
ZTF J164441.18+243428.2	$80.3^{+0.6}_{-0.7}$	$0.614^{+0.011}_{-0.011}$	$0.031^{+0.017}_{-0.015}$	$2.197^{+0.087}_{-0.086}$	2.43 ± 0.22	59283.3945858(11)	0.0801054
ZTF J180256.45−005458.3	$84.2^{+0.3}_{-0.3}$	$1.485^{+0.020}_{-0.023}$	$0.114^{+0.028}_{-0.024}$	$4.700^{+0.077}_{-0.101}$	4.38 ± 0.15	59646.3585478(21)	0.2690033
ZTF J182848.77+230838.0	$88.7^{+0.1}_{-0.3}$	$0.852^{+0.005}_{-0.002}$	$0.088^{+0.014}_{-0.018}$	$4.955^{+0.079}_{-0.077}$	4.914 ± 0.097	59695.37741036(84)	0.1120067
ZTF J195456.71+101937.5	$84.5^{+0.7}_{-0.8}$	$1.901^{+0.020}_{-0.016}$	$0.078^{+0.022}_{-0.023}$	$3.495^{+0.051}_{-0.050}$	3.449 ± 0.057	59697.3389707(12)	0.3102884

5.2 Brown dwarf companions

WDs with brown dwarf companions are rare, with around 0.5 per cent of WDs expected to have substellar partners (Steele et al. 2011). Eclipsing examples are, predictably, even rarer with only four systems currently confirmed (Beuermann et al. 2013; Littlefair et al. 2014; Parsons et al. 2017a; Casewell et al. 2020b; van Roestel et al. 2021). These eclipsing WD-brown dwarf binaries are valuable as they are one of the few places where both the brown dwarf's radii and mass can be measured precisely and are therefore important benchmarks for brown dwarf models. Additionally, as some of the lowest mass objects thought to survive the common-envelope (Casewell et al. 2018), brown dwarfs in PCEBs occupy an important area of the parameter space when studying common-envelope evolution, with the study of the common-envelope phase in this low-mass regime having implications for systems with planetary mass companions (Vanderburg et al. 2020).

In our ULTRACAM follow-up we have found four systems so far that our light curve fits suggest as having brown dwarf companions. These are ZTF J080441.95−021545.7, ZTF J103448.82+005201.9, ZTF J145819.54+131326.7, and ZTF J182848.77+230838.0. As our mass-radius relation for M dwarfs (Brown et al. 2022) is horizontal below 0.07 $M_\odot$ – and therefore uninformative in this regime – the best fit secondary masses can only be regarded as upper limits. Additionally, as none of the secondaries for these systems are detected in-eclipse, only an upper limit can be given for their effective temperatures. One of these systems, ZTF J182848.77+230838.0, has a high secondary temperature for a brown dwarf. In order to rule out problems with the photometry, we stack the in-eclipse images (Figure 4). This reveals a faint (G = 20.88 mag) source 2.79 arcsec away from the target which results in an erroneous slight 'detection' in eclipse and therefore a higher than expected temperature. The true

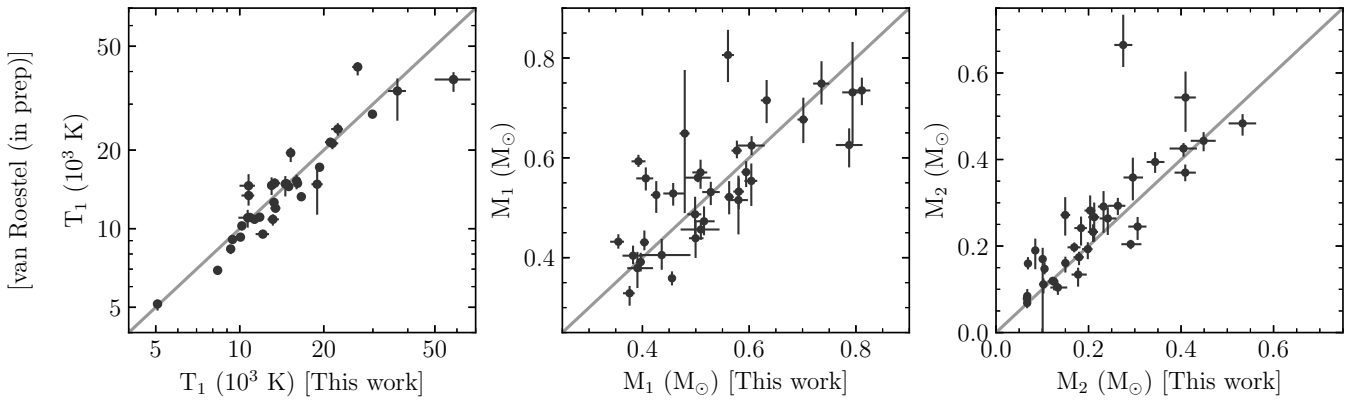

Figure 3. Comparison of our parameters from the NTT-ULTRACAM photometry against the initial parameters of van Roestel et al. (in prep) from ZTF photometry.

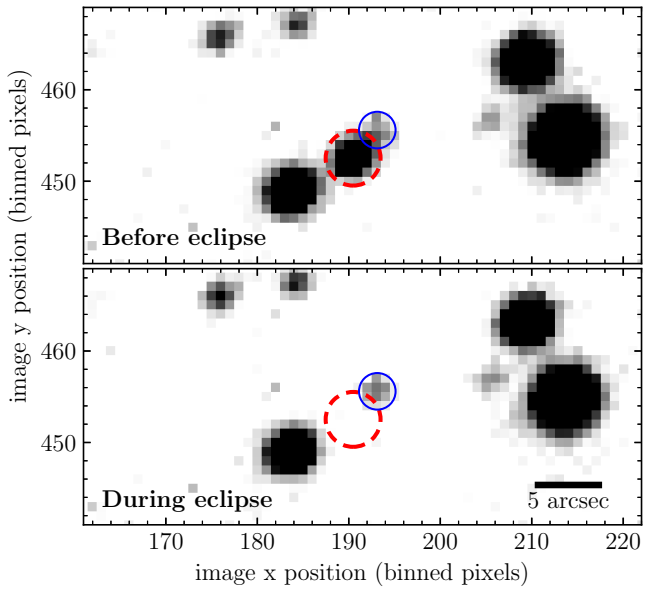

Figure 4. Stacked images of ZTF J1828+2308 taken with ULTRACAM in the i_s filter before and during the eclipse. The red dashed aperture shows the location of ZTF J1828+2308 itself while the solid blue aperture shows the fainter background source 2.79" away (Gaia DR3 4529477702982880512) that is marginally affecting our in-eclipse photometry.

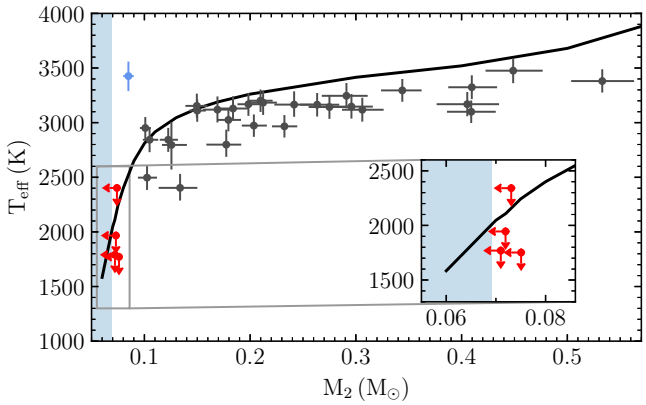

Figure 5. Measured masses and effective temperatures of the M dwarf components with an inset plot zoomed in around the brown dwarfs (which are shown in red). The solid black line shows the 1 Gyr track from Baraffe et al. (2015) and the shaded blue area denotes the region where our mass-radius relation is horizontal (i.e. the radius is constant in this mass range). For the brown dwarfs we plot the masses and temperatures as upper limits centred on the 84$^{\rm th}$ percentile of the fit. The blue point denotes ZTF J1405+1039 which has a best-fit secondary temperature that is much hotter than expected for its mass.

upper limit for the secondary temperature will be lower than given by our fit.

In addition to these four systems with sub-stellar companions, we have measured one system with a companion mass just above the hydrogen-burning limit, ZTF J140537.34+103919.0, hereafter ZTF J1405+1039. The best-fit parameters for this system suggest that the secondary is significantly hotter than would be expected for its mass (shown as the blue point in Figure 5). Again, we stack the in-eclipse images to rule out problems in the photometry (Figure 6), demonstrating that the source is indeed detected in-eclipse. We believe that the most likely explanation for this is that ZTF J1405+1039 is actually a triple system, with a tertiary companion contributing a significant fraction of the in-eclipse flux.

5.3 ZZ Ceti WDs

ZZ Cetis are pulsating WDs, possessing hydrogen atmospheres and pulsation periods ranging from tens of seconds to tens of minutes (Fontaine & Brassard 2008; Winget & Kepler 2008; Romero et al. 2022). The presence of pulsations enable asteroseismological analyses to be performed, providing insight into the internal structure of the WD which is otherwise concealed by their highly stratified nature. In PCEBs, the possibility of measuring the internal structure of the WD is especially interesting as it can reveal how the WD itself is affected by the common-envelope phase (Hermes et al. 2015). Previously, only one ZZ Ceti WD in a detached eclipsing binary was known (Parsons et al. 2020). This system is a double WD binary, however, and as such its evolutionary history is less well defined, with the number of common-envelope events it has passed through being uncertain. ZZ Cetis found in WD-main sequence PCEBs do not have this problem with their evolutionary past known to comprise of a single common-envelope phase. These systems are therefore potentially

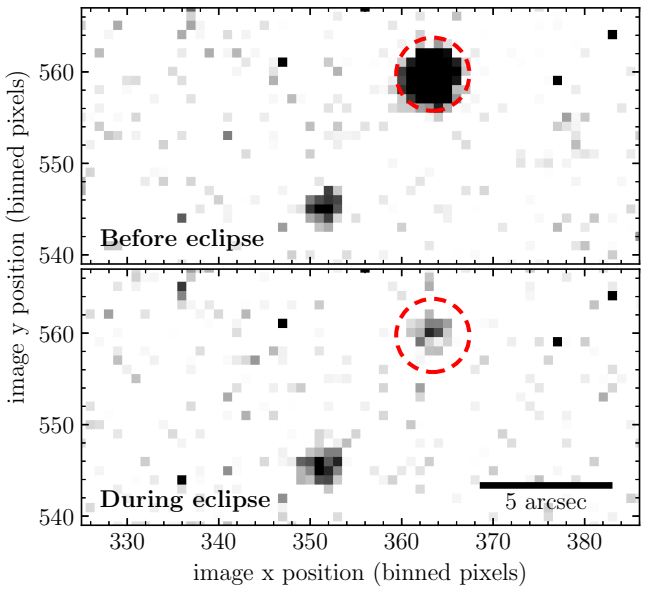

Figure 6. Stacked images of ZTF J1405+1039 taken with ULTRACAM in the i_s filter before and during the eclipse. The red dashed aperture shows the location of ZTF J1405+1039. It is clear that the source is still detected in-eclipse.

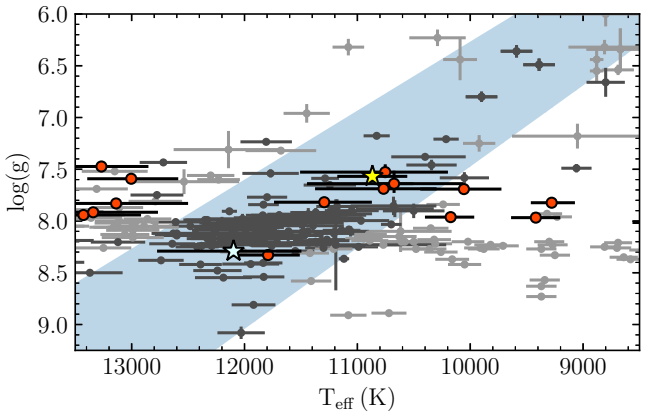

Figure 7. The ZZ Ceti instability strip (blue region) with known pulsating (dark grey) and non-pulsating (light grey) WDs from Gianninas et al. (2011); Steinfadt et al. (2012); Hermes et al. (2012, 2013a,c,b); Romero et al. (2022). Points in red show the measured parameters of the WD components of binaries fit in this work, with the confirmed pulsators, ZTF J1407+2115 and ZTF J0528+2156, shown by the yellow and cyan stars respectively.

very interesting systems to find. Currently there is one known ZZ Ceti WD in a detached, albeit not eclipsing, PCEB (Pyrzas et al. 2015). Although this is an important find, Hermes et al. (2015) noted that there were a lot of free parameters, limiting the precision of the asteroseismological analysis. Eclipsing examples of such systems would reduce these free parameters and enable a more precise analysis.

Comparing our best fit parameters for the WD components to the ZZ Ceti instability strip (Figure 7), we find that eight of our systems have WDs that lie within 1σ of the instability strip (shown in Table 3). Closer inspection of their light curves do not reveal any clear photometric variability indicative of pulsations in six of the

Target	RA	Dec	G	Pulsating
ZTF J0519+0925	05:19:02.1	+09:25:26.38	19.0	Candidate
ZTF J0528+2156	05:28:48.2	+21:56:28.94	17.7	Confirmed
ZTF J0948+2538	09:48:26.4	+25:38:10.68	18.7	Candidate
ZTF J1034+0052	10:34:48.8	+00:52:01.69	19.0	Candidate
ZTF J1302−0032	13:02:28.3	-00:32:00.11	16.8	Candidate
ZTF J1407+2115	14:07:02.6	+21:15:59.75	17.4	Confirmed
ZTF J1634−2713	16:34:21.0	-27:13:21.54	18.8	Candidate
ZTF J1802−0054	18:02:56.4	-00:54:58.47	18.0	Candidate

Table 3. eclipsing PCEBs with – either confirmed or candidate – ZZ Ceti WDs

systems, however, the out-of-eclipse data for many of these systems is typically less than 30 minutes and so is not enough to rule out pulsations either. Although the WD temperatures are not necessarily precise enough to say with certainty whether a particular WD lies within the instability strip or not. Of these eight systems with WDs that lie in the instability strip, we have found two that show clear variability due to pulsations. These represent the first two ZZ Ceti WDs found in eclipsing WD+dM PCEBs.

5.3.1 *ZTF J1407+2115*

ZTF J140702.56+211559.7, hereafter ZTF J1407+2115, was first observed with ULTRACAM in February 2021. Unusual out-of eclipse variation was noticed but the data taken in this run was insufficient to confirm pulsations. We observed ZTF J1407+2115 again for 1 h on the 2$^{\rm nd}$ of March 2022, detecting 3 clear pulsations and confirming it as the first eclipsing detached PCEB containing a ZZ Ceti WD. With this confirmation, we observed ZTF J1407+2115 in two long observing runs on the 4$^{\rm th}$ and 26$^{\rm th}$ of March 2022 using the u_s g_s i_s and u_s g_s r_s filters and lasting $\sim$ 2 h and $\sim$ 5 h respectively (Lomb-scargle periodograms of these two long runs are shown in Figure 8). It is the photometry from the long observing run on the 4$^{\rm th}$ of March that we use to fit the system parameters. We choose this observation primarily for consistency with the modelling performed on the other systems in this work, but also as the wider wavelength range provided by the i_s-band strengthens the constraints on the WD temperature. Additionally, chromospheric variability in the Hα feature can lead to higher scatter of M dwarf fluxes in the r_s-band.

In order to fit the eclipse photometry of this system, the pulsations need to be included in the light curve model to prevent them introducing large systematic errors in the best-fit parameters. We do this using a Gaussian process (GP) implemented through the PYTHON package, GEORGE[5] (Ambikasaran et al. 2015). The GP is applied to the residuals of the PYLCURVE model at each MCMC walker position, with the posterior log probability calculated as the sum of the GP marginalised log likelihood, the log likelihood from comparing the model WD SED with the measured eclipse depths, and the log priors (parallax and interstellar reddening). We use the `ExpSquaredKernel`, defined by an amplitude, temperature, and scale-length, with the temperature scaling the pulsation amplitude between the light curves in different filters according to a blackbody law. These three GP parameters are included as free parameters in our fit. We switch the GP off between the second and third contact points where the WD is totally eclipsed by its M dwarf companion, with the contact points being calculated for every walker position. We then use EMCEE (Foreman-Mackey et al. 2013) to sample from the posterior probability distribution and determine the best-fit parameters. This best-fit model is shown in Figure 9.

[5] https://george.readthedocs.io/en/latest/

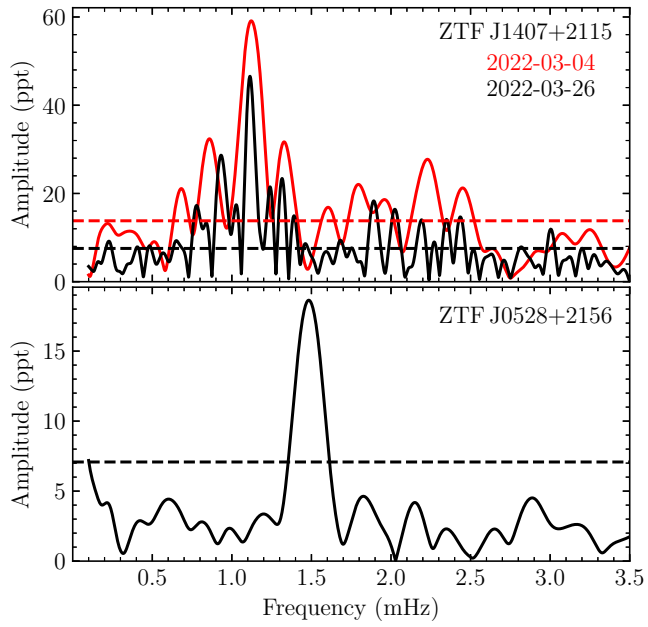

Figure 8. Lomb-Scargle periodograms (shown in parts per thousand relative to the flux of the WD) of the ULTRACAM g_s light curves of ZTF J1407+2115 and ZTF J0528+2156 with their respective eclipse light curve models subtracted. Horizontal dashed lines show the 3σ significance levels calculated using the bootstrapping method described by Greiss et al. (2014, Section 4.1).

We find the WD to have an effective temperature of 10 900 ± 300 K and a mass of 0.41 ± 0.01 $M_\odot$, suggesting a core composed primarily of helium. This mass and temperature corresponds to a surface gravity of 7.57 ± 0.04 dex, placing it in a relatively sparsely sampled region in the middle of the instability strip (Figure 7).

We subtract our best-fit eclipse light curve model from the g_s-band photometry of the longer run on the 26$^{\rm th}$ of March, leaving just the pulsation signal. Running a periodogram on this determines the main pulsation mode to have a frequency of 1.11 mHz (898 s) with an amplitude of around 47 parts per thousand (ppt) (Figure 8). We calculate the 3σ significance threshold to be 8 ppt following the method of Greiss et al. (2014), shuffling the flux values 10 000 times and taking the amplitude of the 99.7$^{\rm th}$ percentile highest peak.

5.3.2 ZTF J0528+2156

ZTF J052848.24+215629.0, hereafter ZTF J0528+2156, was first observed with ULTRACAM in February 2021. Attempts at fitting the eclipse light curve showed some possible structure in the residuals, prompting us to observe it again to search for pulsations. We observed ZTF J0528+2156 again on the 18$^{\rm th}$ of December 2022 for 1.8 h, detecting pulsations with a period of around 11 minutes and amplitude of around 5 per cent.

We fit the ULTRACAM photometry in the same way as for ZTF J1407+2115 – using a Gaussian process to model the pulsations. We find the WD to have an effective temperature of 11 900 ± 600 K and a mass of 0.78 ± 0.02 $M_\odot$, corresponding to a surface gravity of 8.27 ± 0.044 dex and placing it comfortably within the instability strip (Figure 7). Computing the periodogram of the residuals of the eclipse light curve model in the same way as for ZTF J1407+2115, we find the main mode to have a frequency of 1.5 mHz (670 s) and amplitude of around 19 ppt with a 3σ significance threshold of 7 ppt (Figure 8).

5.4 Magnetic WDs

Around 36 per cent of WDs in cataclysmic variables (CVs) are observed to be strongly magnetic (Pala et al. 2020). This is in stark contrast with their progenitor population – the detached PCEBs – of which only a handful possess WDs with strong magnetic fields. Schreiber et al. (2021) propose an evolutionary channel between the magnetic CVs and the detached magnetic population to explain this discrepancy. This relies on a rotation-driven dynamo in which a crystallising WD, spun up due to accretion during the CV phase, can generate the strong magnetic fields that we observe in CVs. Interactions between the newly-formed magnetic field of the WD and the magnetic field of the M dwarf then act to detach the binary, halting mass transfer and causing the binary to appear as a strongly magnetic detached PCEB for a period of time before angular momentum loss due to magnetic braking and gravitational wave radiation brings the two stars back into a mass-transferring state as a polar or intermediate polar.

A test of this model was performed by Parsons et al. (2021), using spectroscopic observations of detached magnetic PCEBs to constrain their evolutionary history, attempting to assess whether or not they are consistent with having undergone a mass-transferring phase in the past. All systems studied were found to be consistent with a previous CV phase but spectroscopic observations alone were not powerful enough to draw strong conclusions. More powerful constraints can be made if such systems are found to be eclipsing, enabling more precise measurements to be made from the eclipse photometry and therefore a robust test of the model.

As part of our follow-up program we have discovered 6 new eclipsing PCEBs (Table 4) that we have confirmed from our high-speed photometry as having magnetic WDs – showing clear evidence of a bright magnetic pole in the eclipse ingress/egress, with one previously known as a magnetic system but not known to be eclipsing. We have additionally found 3 candidate systems that show out-of-eclipse variation that disappears when the WD is eclipsed but for which the ingress/egress of the eclipse do not confirm a bright magnetic pole. These systems have been found by searching for unusual out-of-eclipse variation in their ZTF light curves (Figure 10), inconsistent with the ellipsoidal modulation or reflection effect that is common in PCEBs. This unusual out-of-eclipse variability was noted in the pre-intermediate polar, SDSS J0303+0054, (Parsons et al. 2013) and is due to additional emission in the form of cyclotron radiation from the magnetic poles of the WD. The effect of the cyclotron emission on the eclipse profiles – introducing steps in the ingress and egress due to the eclipse of the small, bright magnetic pole (Figure 10) – makes the light curves of the magnetic systems more complicated to fit and so the analysis of these systems will be the subject of a future paper.

6 CONCLUSIONS

Through our dedicated program of high-speed photometric follow-up we have obtained multi-band eclipse light curves for 43 new PCEBs found using ZTF. We have characterized 34 of these systems from the eclipse light curves alone – finding four that contain sub-stellar companions, doubling the number of eclipsing examples known, and two with pulsating WDs representing the first ZZ Ceti WDs known in eclipsing WD+dM binaries. Of the remaining nine systems, we

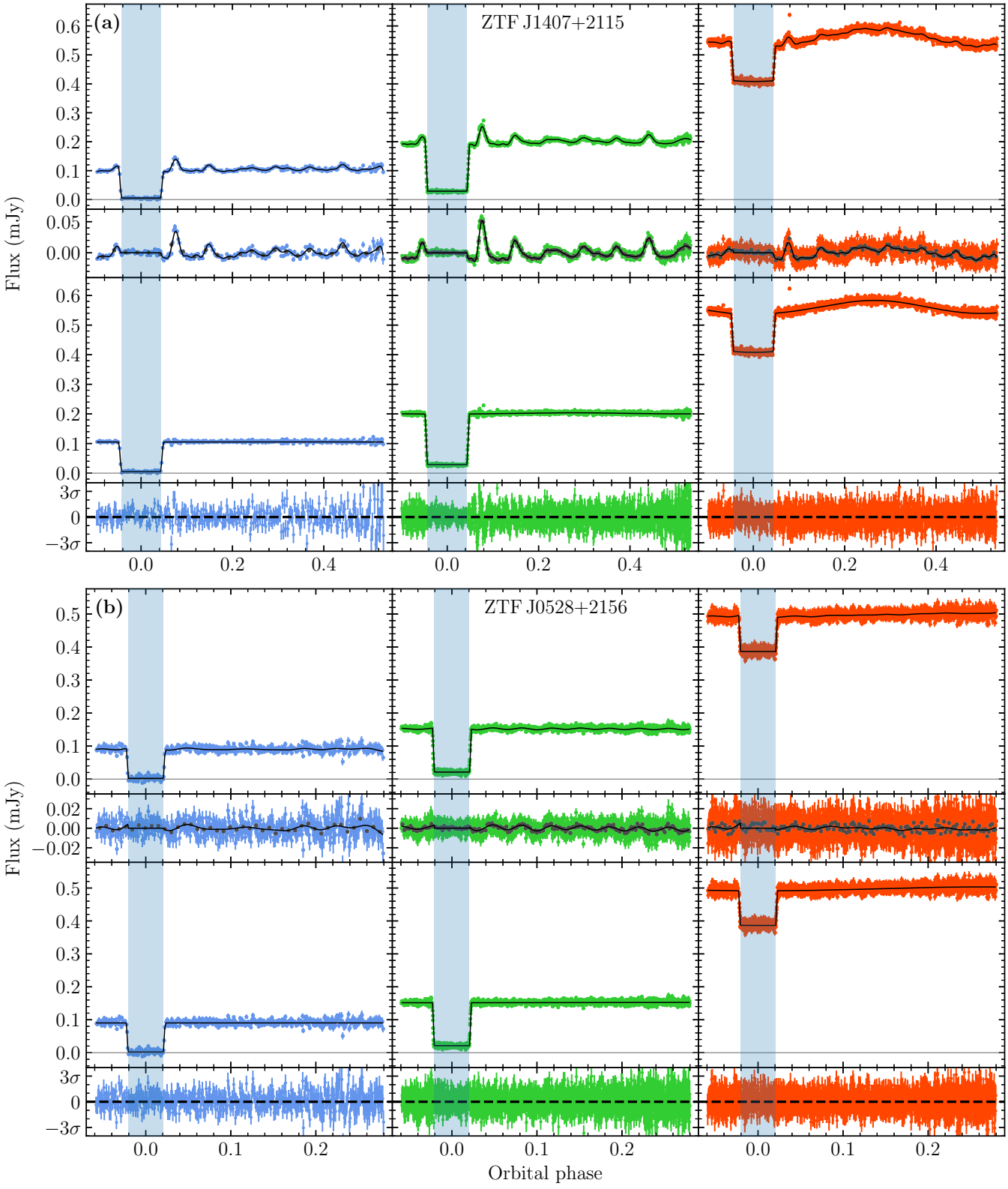

Figure 9. ULTRACAM $u_s\, g_s\, i_s$ light curves of ZTF J1407+2115 (**a**) and ZTF J0528+2156 (**b**). The top row of each plot shows the observed light curve (coloured points) with the combined eclipse plus mean Gaussian process pulsation model (black line). The second row shows the observed light curve with the eclipse model subtracted (coloured points) as well as the same data binned up by a factor of ten (dark grey points) with the mean Gaussian process model (black line). The third row shows the observed light curve with the mean Gaussian process subtracted with the black line showing the eclipse model. The bottom row shows the residuals of the full light curve model. The filled region shows the phase range where the Gaussian process is switched off (between the second and third eclipse contact points).

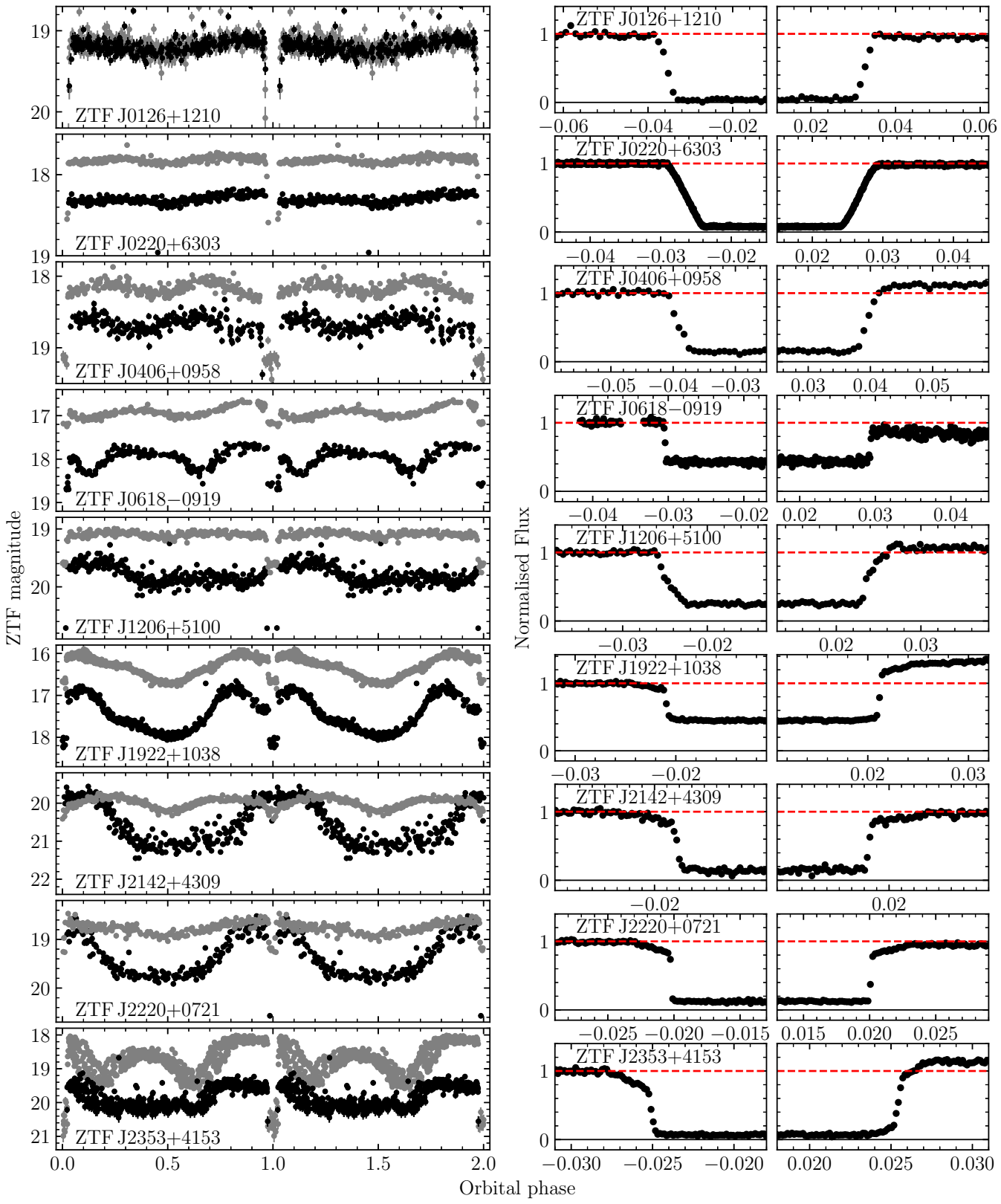

Figure 10. *left*: ZTF g-band (black) and r-band (grey) light curves of the 6 new confirmed, and 3 new candidate eclipsing PCEBs with magnetic WDs. All show out-of-eclipse variation inconsistent with reflection effect or ellipsoidal modulation in at least one filter. Some light curves have been binned for clarity. *right*: Normalised ULTRACAM/HiPERCAM g_s-band primary eclipse light curves (zoomed in on the ingress and egress) of the 6 new confirmed, and 3 new candidate eclipsing PCEBs with magnetic WDs. The solid grey line shows a flux of zero while the red dashed line shows the mean flux of the first 10 points shown.

Target	RA	Dec	G	Magnetic
ZTF J0126+1210	01:26:07.8	+12:10:49.14	18.8	Candidate
ZTF J0220+6303	02:20:04.6	+63:03:59.63	17.4	Candidate
ZTF J0406+0958	04:06:27.2	+09:58:26.97	18.1	Candidate
ZTF J0618−0919	06:18:09.9	−09:19:04.28	16.5	Confirmed
ZTF J1206+5100	12:06:15.7	+51:00:46.77	18.6	Confirmed
ZTF J1922+1038	19:22:15.3	+10:38:38.13	16.0	Confirmed
ZTF J2142+4309	21:42:32.0	+43:09:28.97	19.3	Confirmed
ZTF J2220+0721	22:20:07.5	+07:21:29.74	18.3	Confirmed
ZTF J2353+4153	23:53:55.0	+41:53:04.40	18.7	Confirmed

Table 4. eclipsing PCEBs with – either confirmed or candidate – magnetic WD components.

have found six to contain strongly magnetic WDs from their eclipse photometry with three further candidates. These will be invaluable to the study of magnetic field generation in binary WDs. Our results demonstrate that a photometric approach to the follow-up of eclipsing systems can effectively discern interesting sub-types of PCEBs, including those that would be otherwise missed by spectroscopic follow-up.

ACKNOWLEDGEMENTS

SGP acknowledges the support of the UK's Science and Technology Facilities Council (STFC) Ernest Rutherford Fellowship. ARM acknowledges support from Grant RYC-2016-20254 funded by MCIN/AEI/10.13039/501100011033 and by ESF Investing in your future and from MINECO under the PID2020-117252GB-I00 grant. VSD, HiPERCAM, and ULTRACAM are supported by the STFC. IP and TRM acknowledge support from the STFC, grant ST/T000406/1 and a Leverhulme Research Fellowship. JM was supported by funding from a Science and Technology Facilities Council (STFC) studentship. Based on observations collected at the European Southern Observatory under ESO programme 0106.D-0824. Based on observations made with the Gran Telescopio Canarias (GTC), installed in the Spanish Observatorio del Roque de los Muchachos of the Instituto de Astrofísica de Canarias, in the island of La Palma. This work has made use of data from the European Space Agency (ESA) mission *Gaia* (`https://www.cosmos.esa.int/gaia`), processed by the *Gaia* Data Processing and Analysis Consortium (DPAC, `https://www.cosmos.esa.int/web/gaia/dpac/consortium`). Funding for the DPAC has been provided by national institutions, in particular the institutions participating in the *Gaia* Multilateral Agreement. For the purpose of open access, the author has applied a Creative Commons Attribution (CC BY) licence to any Author Accepted Manuscript version arising. We thank the anonymous referee for their helpful comments.

DATA AVAILABILITY

The data underlying this article will be shared upon reasonable request to the corresponding author.

REFERENCES

Allard F., Homeier D., Freytag B., Sharp C. M., 2012, in Reylé C., Charbonnel C., Schultheis M., eds, EAS Publications Series Vol. 57, EAS Publications Series. pp 3–43 (arXiv:1206.1021), doi:10.1051/eas/1257001

Ambikasaran S., Foreman-Mackey D., Greengard L., Hogg D. W., O'Neil M., 2015, IEEE Transactions on Pattern Analysis and Machine Intelligence, 38, 252

Baraffe I., Homeier D., Allard F., Chabrier G., 2015, A&A, 577, A42

Bédard A., Bergeron P., Brassard P., Fontaine G., 2020, ApJ, 901, 93

Bellm E. C., et al., 2019, PASP, 131, 018002

Best W. M. J., Liu M. C., Magnier E. A., Dupuy T. J., 2021, AJ, 161, 42

Beuermann K., et al., 2013, A&A, 558, A96

Blouin S., Dufour P., Allard N. F., 2018, ApJ, 863, 184

Brown A. J., et al., 2022, MNRAS, 513, 3050

Casewell S. L., et al., 2018, MNRAS, 476, 1405

Casewell S. L., et al., 2020a, MNRAS, 497, 3571

Casewell S. L., Debes J., Braker I. P., Cushing M. C., Mace G., Marley M. S., Kirkpatrick J. D., 2020b, MNRAS, 499, 5318

Claret A., Cukanovaite E., Burdge K., Tremblay P. E., Parsons S., Marsh T. R., 2020, A&A, 641, A157

Copperwheat C. M., Marsh T. R., Dhillon V. S., Littlefair S. P., Hickman R., Gänsicke B. T., Southworth J., 2010, MNRAS, 402, 1824

Dhillon V. S., et al., 2007, MNRAS, 378, 825

Dhillon V. S., et al., 2021, MNRAS, 507, 350

Eggleton P. P., Tokovinin A. A., 2008, MNRAS, 389, 869

Fontaine G., Brassard P., 2008, PASP, 120, 1043

Foreman-Mackey D., Hogg D. W., Lang D., Goodman J., 2013, PASP, 125, 306

Gianninas A., Bergeron P., Ruiz M. T., 2011, ApJ, 743, 138

Graham M. J., et al., 2019, PASP, 131, 078001

Greiss S., Gänsicke B. T., Hermes J. J., Steeghs D., Koester D., Ramsay G., Barclay T., Townsley D. M., 2014, MNRAS, 438, 3086

Hermes J. J., Montgomery M. H., Winget D. E., Brown W. R., Kilic M., Kenyon S. J., 2012, ApJ, 750, L28

Hermes J. J., et al., 2013a, MNRAS, 436, 3573

Hermes J. J., et al., 2013b, ApJ, 765, 102

Hermes J. J., Kepler S. O., Castanheira B. G., Gianninas A., Winget D. E., Montgomery M. H., Brown W. R., Harrold S. T., 2013c, ApJ, 771, L2

Hermes J. J., et al., 2015, MNRAS, 451, 1701

Hernandez M. S., et al., 2022, MNRAS, 512, 1843

Husser T. O., Wende-von Berg S., Dreizler S., Homeier D., Reiners A., Barman T., Hauschildt P. H., 2013, A&A, 553, A6

Ivezić Ž., et al., 2019, ApJ, 873, 111

Jones D., Boffin H. M. J., 2017, Nature Astronomy, 1, 0117

Kosakowski A., Kilic M., Brown W. R., Bergeron P., Kupfer T., 2022, MNRAS, 516, 720

Littlefair S. P., et al., 2014, MNRAS, 445, 2106

Masci F. J., et al., 2019, PASP, 131, 018003

Morrell S., Naylor T., 2019, MNRAS, 489, 2615

Naylor T., 1998, MNRAS, 296, 339

O'Brien M. S., Bond H. E., Sion E. M., 2001, ApJ, 563, 971

Paczynski B., 1976, in Eggleton P., Mitton S., Whelan J., eds, IAU Symposium Vol. 73, Structure and Evolution of Close Binary Systems. p. 75

Pala A. F., et al., 2020, MNRAS, 494, 3799

Panei J. A., Althaus L. G., Chen X., Han Z., 2007, MNRAS, 382, 779

Parsons S. G., et al., 2013, MNRAS, 429, 256

Parsons S. G., et al., 2015, MNRAS, 449, 2194

Parsons S. G., Rebassa-Mansergas A., Schreiber M. R., Gänsicke B. T., Zorotovic M., Ren J. J., 2016, MNRAS, 463, 2125

Parsons S. G., et al., 2017a, MNRAS, 470, 4473

Parsons S. G., et al., 2017b, MNRAS, 471, 976

Parsons S. G., et al., 2018, MNRAS, 481, 1083

Parsons S. G., et al., 2020, Nature Astronomy, 4, 690

Parsons S. G., Gänsicke B. T., Schreiber M. R., Marsh T. R., Ashley R. P., Breedt E., Littlefair S. P., Meusinger H., 2021, MNRAS, 502, 4305

Pyrzas S., et al., 2015, MNRAS, 447, 691

Raghavan D., et al., 2010, ApJS, 190, 1

Rebassa-Mansergas A., Gänsicke B. T., Rodríguez-Gil P., Schreiber M. R., Koester D., 2007, MNRAS, 382, 1377

Rebassa-Mansergas A., Gänsicke B. T., Schreiber M. R., Koester D., Rodríguez-Gil P., 2010, MNRAS, 402, 620

Rebassa-Mansergas A., Nebot Gómez-Morán A., Schreiber M. R., Gänsicke B. T., Schwope A., Gallardo J., Koester D., 2012, MNRAS, 419, 806
Rebassa-Mansergas A., Ren J. J., Parsons S. G., Gänsicke B. T., Schreiber M. R., García-Berro E., Liu X. W., Koester D., 2016, MNRAS, 458, 3808
Rebassa-Mansergas A., et al., 2017, MNRAS, 472, 4193
Rebassa-Mansergas A., Parsons S. G., Dhillon V. S., Ren J., Littlefair S. P., Marsh T. R., Torres S., 2019, Nature Astronomy, 3, 553
Rebassa-Mansergas A., et al., 2021, MNRAS, 506, 5201
Romero A. D., et al., 2022, MNRAS, 511, 1574
Saumon D., Marley M. S., 2008, ApJ, 689, 1327
Schreiber M. R., Belloni D., Gänsicke B. T., Parsons S. G., Zorotovic M., 2021, Nature Astronomy, 5, 648
Steele P. R., Burleigh M. R., Dobbie P. D., Jameson R. F., Barstow M. A., Satterthwaite R. P., 2011, MNRAS, 416, 2768
Steinfadt J. D. R., Bildsten L., Kaplan D. L., Fulton B. J., Howell S. B., Marsh T. R., Ofek E. O., Shporer A., 2012, PASP, 124, 1
Tremblay P. E., Bergeron P., Gianninas A., 2011, ApJ, 730, 128
Vanderburg A., et al., 2020, Nature, 585, 363
Willems B., Kolb U., 2004, A&A, 419, 1057
Winget D. E., Kepler S. O., 2008, ARA&A, 46, 157
van Roestel J., et al., 2021, ApJ, 919, L26

APPENDIX A: OBSERVATIONS

APPENDIX B: LIGHT CURVES

This paper has been typeset from a TEX/LATEX file prepared by the author.

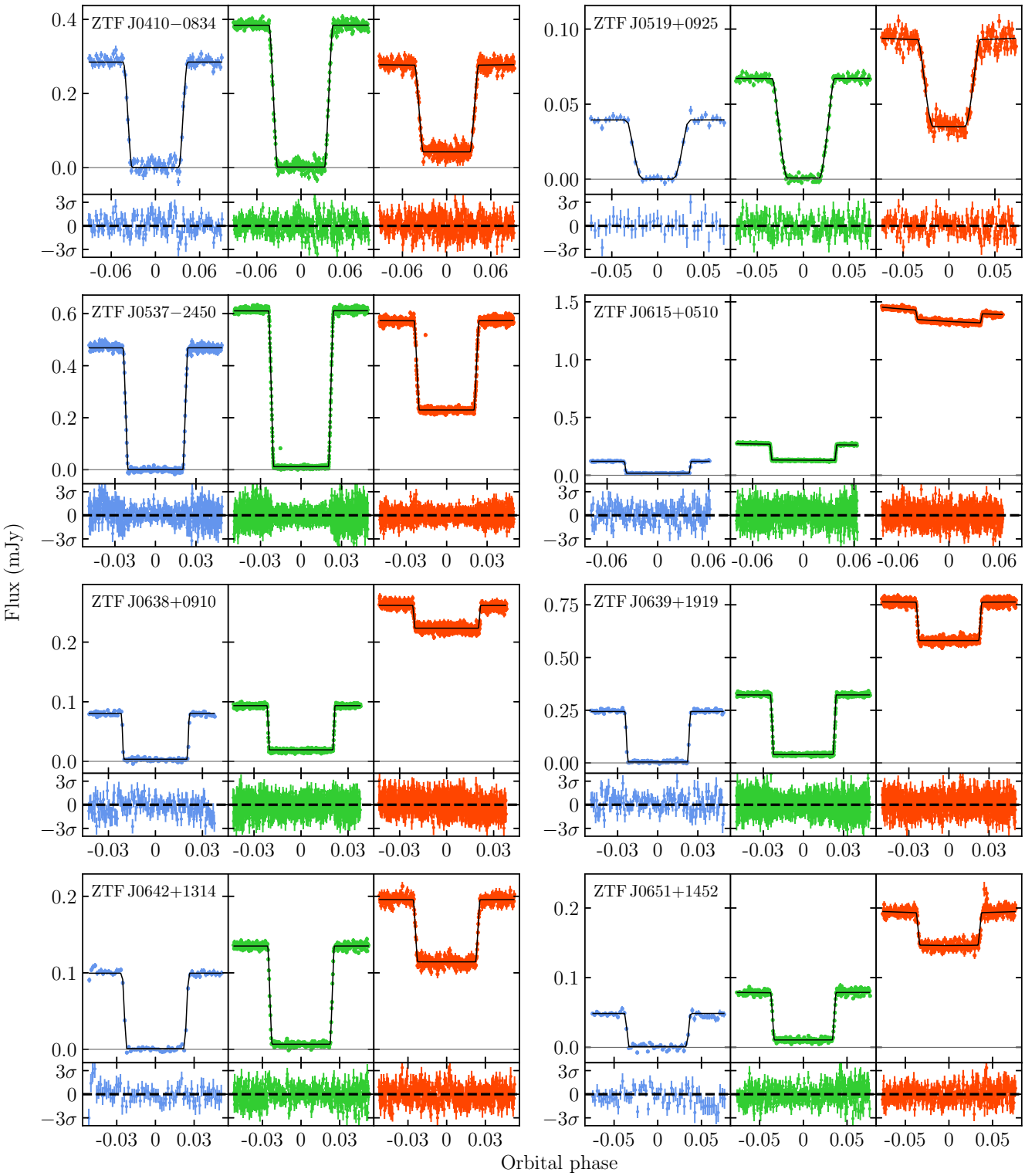

Figure B1. Best-fit light curve models (solid black lines) to the ULTRACAM u_s g_s i_s eclipse photometry (coloured points) of the non-pulsating systems. The horizontal grey lines show a flux of zero. Residuals of the best-fit models are shown in the panels below the light curves.

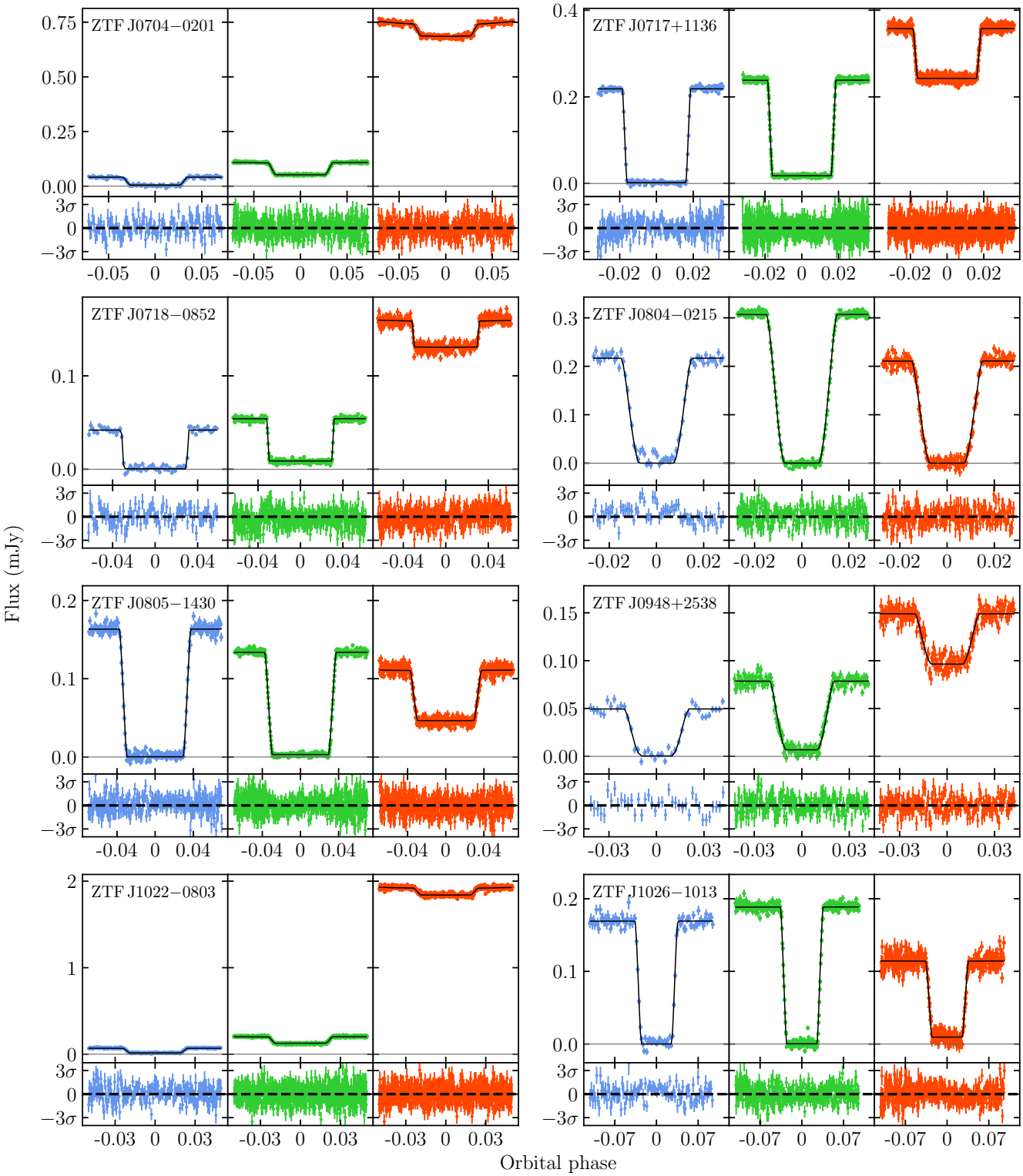

Figure B2. As in Figure B1.

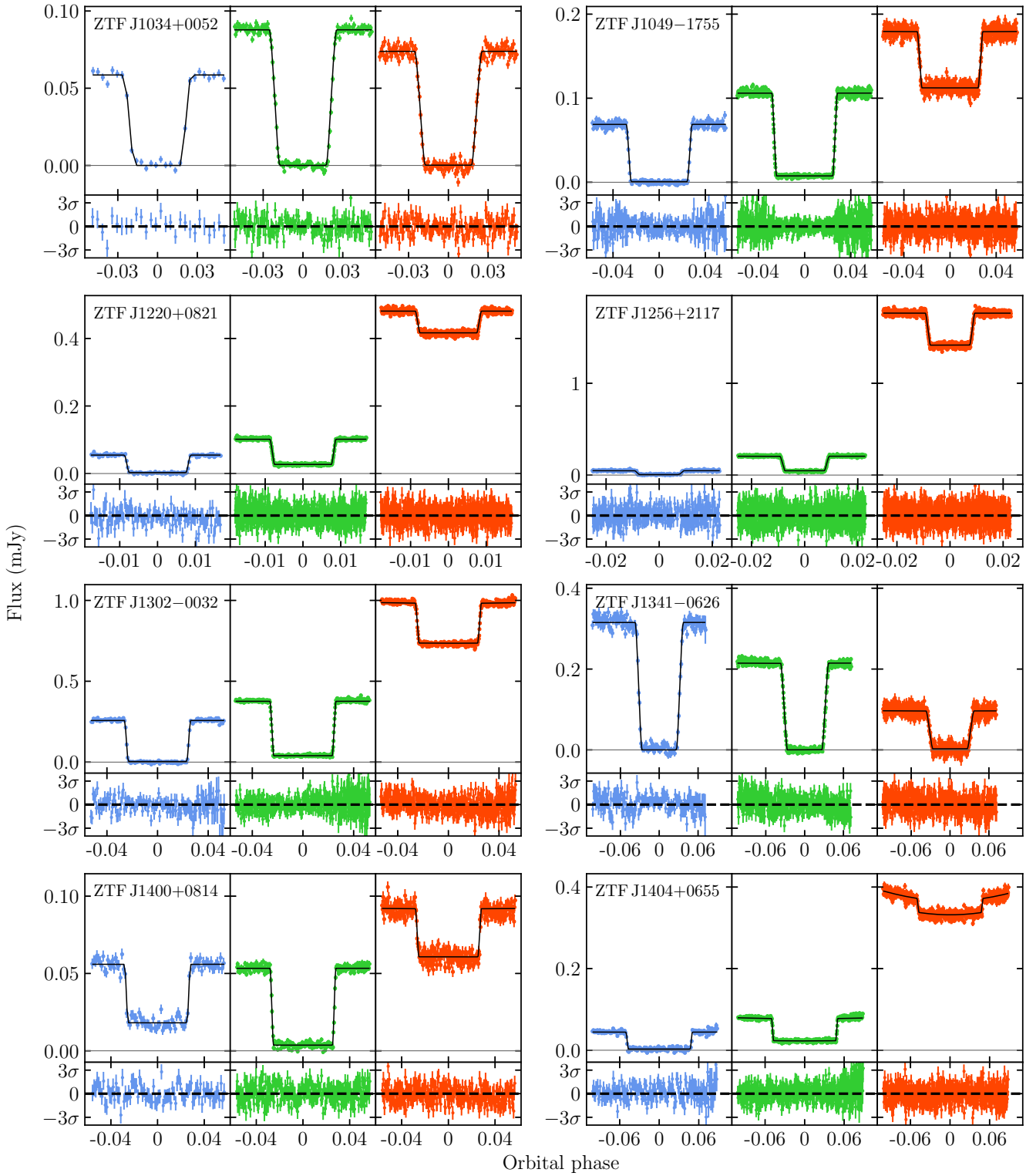

Figure B3. As in Figure B1.

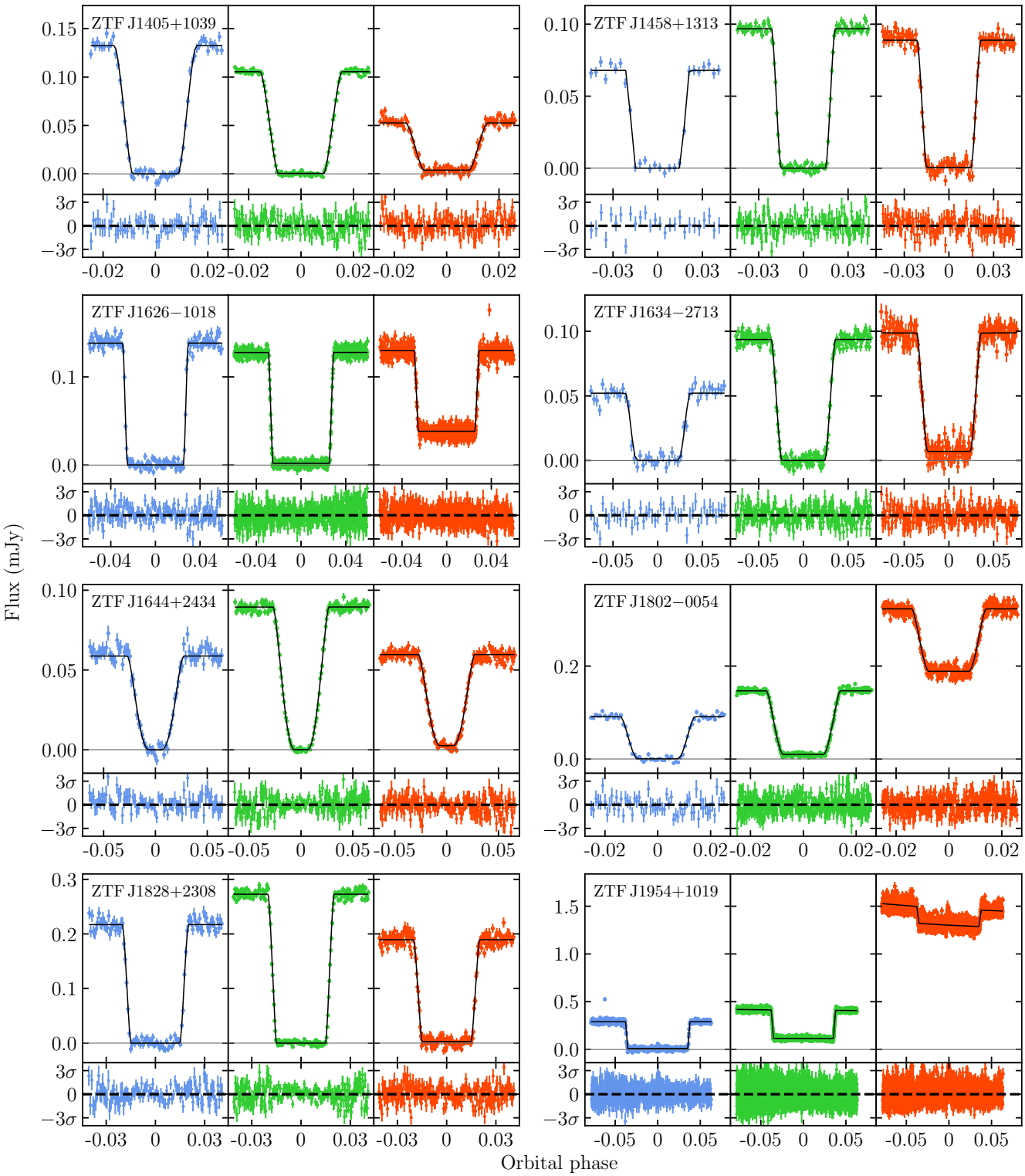

Figure B4. As in Figure B1.

Target	Date at start of run	Start (UT)	Telescope-Instrument	Filters	Exposure time (s)	Number of exposures	Conditions (Transparency, seeing)
ZTF J012607.79+121049.1	2021-07-08	09:03:28	NTT-ULTRACAM	$u_s g_s i_s$	7.0	804	clear, ~1 arcsec
ZTF J022004.55+630359.6	2021-08-07	04:40:29	GTC-HiPERCAM	$u_s g_s r_s i_s z_s$	0.7	3568	clear, ~0.6 arcsec
ZTF J040627.23+095827.0	2021-02-08	01:10:49	NTT-ULTRACAM	$u_s g_s i_s$	7.5	269	clear, <1.5 arcsec
	2021-11-08	02:54:14	NTT-ULTRACAM	$u_s g_s i_s$	8.0	1426	clear, ~1 arcsec
	2021-11-10	06:25:25	NTT-ULTRACAM	$u_s g_s r_s$	8.0	712	clear, <1.5 arcsec
	2021-09-13	02:10:27	GTC-HiPERCAM	$u_s g_s r_s i_s z_s$	1.2	3183	clear, <2.0 arcsec
ZTF J041016.82−083419.5	2022-03-08	00:51:41	NTT-ULTRACAM	$u_s g_s i_s$	3.8	528	clear, <1.8 arcsec
ZTF J051902.06+092526.4	2021-02-06	00:59:07	NTT-ULTRACAM	$u_s g_s i_s$	8.0	156	clear, <1.5 arcsec
ZTF J052848.24+215629.0	2021-02-08	01:51:58	NTT-ULTRACAM	$u_s g_s i_s$	4.0	632	clear, <1.4 arcsec
	2022-12-19	04:41:40	NTT-ULTRACAM	$u_s g_s i_s$	3.7	1806	clear, <2 arcsec
ZTF J053708.26−245014.6	2021-02-06	04:42:38	NTT-ULTRACAM	$u_s g_s i_s$	3.0	1386	clear, <1.3 arcsec
ZTF J061530.96+051041.8	2021-03-07	02:01:48	NTT-ULTRACAM	$u_s g_s i_s$	6.8	774	clear, <1.4 arcsec
ZTF J061809.92−091904.3	2022-12-19	01:07:56	NTT-ULTRACAM	$u_s g_s i_s$	4.5	690	clear, ~1.3 arcsec
	2022-12-19	08:00:21	NTT-ULTRACAM	$u_s g_s i_s$	3.4	474	clear, ~1.3 arcsec
ZTF J063808.71+091027.4	2021-02-07	02:57:13	NTT-ULTRACAM	$u_s g_s i_s$	7.0	656	clear, <1.2 arcsec
ZTF J063954.70+191958.0	2021-02-06	03:34:25	NTT-ULTRACAM	$u_s g_s i_s$	3.0	1300	clear, ~1.3 arcsec
ZTF J064242.41+131427.6	2021-02-07	01:52:06	NTT-ULTRACAM	$u_s g_s i_s$	4.5	591	clear, ~1 arcsec
ZTF J065103.70+145246.2	2021-02-07	04:36:41	NTT-ULTRACAM	$u_s g_s i_s$	7.0	359	clear, ~1.5 arcsec
ZTF J070458.08−020103.3	2021-02-08	04:45:27	NTT-ULTRACAM	$u_s g_s i_s$	6.0	411	clear, <1.5 arcsec
ZTF J071759.04+113630.2	2021-02-06	02:39:58	NTT-ULTRACAM	$u_s g_s i_s$	4.0	666	clear, <1.3 arcsec
ZTF J071843.68−085232.1	2021-03-10	01:54:13	NTT-ULTRACAM	$u_s g_s i_s$	7.5	379	clear, <1.2 arcsec
ZTF J080441.95−021545.7	2022-03-08	01:43:23	NTT-ULTRACAM	$u_s g_s i_s$	3.1	736	clear, ~1.7 arcsec
ZTF J080542.98−143036.3	2022-03-08	03:30:59	NTT-ULTRACAM	$u_s g_s i_s$	6.0	757	clear, ~1 arcsec
ZTF J094826.35+253810.6	2021-01-25	05:43:23	NTT-ULTRACAM	$u_s g_s i_s$	6.5	602	clear, ~1 arcsec
ZTF J102254.00−080327.3	2021-03-07	05:35:30	NTT-ULTRACAM	$u_s g_s i_s$	4.0	1224	clear, <1.4 arcsec
ZTF J102653.47−101330.3	2021-01-23	05:28:43	NTT-ULTRACAM	$u_s g_s i_s$	5.8	316	clear, ~2 arcsec
ZTF J103448.82+005201.9	2021-02-08	05:33:49	NTT-ULTRACAM	$u_s g_s i_s$	5.8	408	clear, ~1 arcsec
ZTF J104906.96−175530.7	2021-01-24	08:01:57	NTT-ULTRACAM	$u_s g_s i_s$	4.5	866	clear, ~1 arcsec
ZTF J120615.74+510046.8	2021-05-08	21:54:23	GTC-HiPERCAM	$u_s g_s r_s i_s z_s$	5.4	9509	thin cloud, ~2 arcsec
ZTF J122009.98+082155.0	2021-02-07	05:28:34	NTT-ULTRACAM	$u_s g_s i_s$	7.0	536	clear, <1.6 arcsec
ZTF J125620.57+211725.8	2022-03-03	07:38:55	NTT-ULTRACAM	$u_s g_s i_s$	2.5	1440	clear, ~1 arcsec
ZTF J130228.34−003200.2	2021-02-07	08:39:46	NTT-ULTRACAM	$u_s g_s i_s$	4.0	692	clear, ~1 arcsec
ZTF J134151.70−062613.9	2021-01-23	06:19:18	NTT-ULTRACAM	$u_s g_s i_s$	3.5	1216	clear, ~1.8 arcsec
ZTF J140036.65+081447.4	2021-02-08	06:15:28	NTT-ULTRACAM	$u_s g_s i_s$	10.0	434	clear, ~1 arcsec
ZTF J140423.86+065557.7	2021-01-25	07:56:09	NTT-ULTRACAM	$u_s g_s i_s$	6.0	705	clear, ~1 arcsec
ZTF J140537.34+103919.0	2021-02-06	07:28:35	NTT-ULTRACAM	$u_s g_s i_s$	10.0	276	clear, ~1.2 arcsec
ZTF J140702.57+211559.7	2021-02-07	07:22:27	NTT-ULTRACAM	$u_s g_s i_s$	4.5	468	clear, ~1.2 arcsec
	2022-03-05	07:35:10	NTT-ULTRACAM	$u_s g_s i_s$	6.0	1304	clear, ~1 arcsec
	2022-03-27	04:07:31	NTT-ULTRACAM	$u_s g_s r_s$	5.0	3455	clear, ~1.1 arcsec
ZTF J145819.54+131326.7	2021-02-07	08:05:49	NTT-ULTRACAM	$u_s g_s i_s$	6.5	284	clear, ~1 arcsec
ZTF J162644.18−101854.3	2021-02-08	08:18:21	NTT-ULTRACAM	$u_s g_s i_s$	5.0	660	clear, ~1.3 arcsec
ZTF J163421.00−271321.7	2021-02-08	07:35:28	NTT-ULTRACAM	$u_s g_s i_s$	5.4	420	clear, ~1.2 arcsec
ZTF J164441.18+243428.2	2021-03-10	09:06:00	NTT-ULTRACAM	$u_s g_s i_s$	6.0	321	clear, ~1.0 arcsec
ZTF J180256.45−005458.3	2022-03-08	08:08:10	NTT-ULTRACAM	$u_s g_s i_s$	4.0	728	clear, ~1.2 arcsec
ZTF J182848.77+230838.0	2022-04-26	09:09:02	NTT-ULTRACAM	$u_s g_s i_s$	4.0	532	clear, ~2 arcsec
ZTF J192215.32+103838.1	2022-06-07	06:46:35	NTT-ULTRACAM	$u_s g_s i_s$	3.9	803	thin cloud, ~1 arcsec
ZTF J195456.71+101937.5	2022-04-28	07:19:49	NTT-ULTRACAM	$u_s g_s i_s$	1.4	3174	clear, <2.5 arcsec
ZTF J214232.02+430929.0	2021-09-06	23:17:08	GTC-HiPERCAM	$u_s g_s r_s i_s z_s$	2.0	1544	clear, ~1 arcsec
ZTF J222007.49+072129.7	2021-09-11	00:04:54	GTC-HiPERCAM	$u_s g_s r_s i_s z_s$	0.7	4047	some clouds, ~0.8 arcsec
ZTF J235354.98+415304.4	2021-09-09	04:43:15	GTC-HiPERCAM	$u_s g_s r_s i_s z_s$	1.0	2770	clear, ~0.6 arcsec

Table A1. Journal of observations.